Brightness temperature simulation of subarctic lake-ice evolution by HIGHTSI and SMRT model

ZHANG Yixiao[1,2,3], QIU Yubao[1,2,3*], PENG Chongtai[4], Bin CHENG[5], SHI Lijuan[1,6,7] & Matti LEPPÄRANTA[1,8]

[1] Key Laboratory of Digital Earth Science, Aerospace Information Research Institute, Chinese Academy of Sciences, Beijing 100094, China;

[2] International Research Center of Big Data for Sustainable Development Goals, Beijing 100094, China;

[3] University of Chinese Academy of Sciences, Beijing 100049, China;

[4] School of Information and Communication, Guilin University of Electronic Technology, Guilin 541004, China;

[5] Finnish Meteorological Institute, Helsinki 00101, Finland;

[6] National Key Laboratory of Microwave Imaging Technology, Aerospace Information Research Institute, Chinese Academy of Sciences, Beijing 100094, China;

[7] Department of Space Microwave Remote Sensing System, Aerospace Information Research Institute, Chinese Academy of Sciences, Beijing 100094, China;

[8] University of Helsinki, Helsinki 00014, Finland

Abstract   Microwave brightness temperature (TB) can be used to retrieve lake ice thickness in the Arctic and subarctic regions. However, the accuracy of the retrieval is affected by the physical properties of lake ice. To improve the understanding of how lake ice affects TB, numerical modeling was applied. This study combined a physical thermodynamic ice model HIGHTSI with a microwave radiation transfer model SMRT to simulate the TB and lake ice evolution in 2002–2011 in Hulun Lake, China. The reanalyzed meteorological data were used as atmospheric forcing. The ice season was divided into the growth period, the slow growth period, and the ablation period. The simulations revealed that TB was highly sensitive to ice thickness during the ice season, especially vertical polarization measurement at 18.7 GHz. The quadratic polynomial fit for ice thickness to TB outperformed the linear fit, regardless of whether lake ice contained bubbles or not. A comparison of the simulated TB with space-borne TB showed that the simulated TB had the best accuracy during the slow growth period, with a minimum RMSE of 4.6 K. The results were influenced by the bubble radius and salinity. These findings enhance comprehension of the interaction between lake ice properties (including ice thickness, bubbles, and salinity) and TB during ice seasons, offering insights to sea ice in the Arctic and subarctic freshwater observations.

Keywords   lake ice evolution, HIGHTSI, SMRT, ice thickness, passive microwave brightness temperature

1   Introduction

Globally, more than fifty million lakes are seasonally affected by ice, the southern limit extends to 30°N in China (Sharma et al., 2019; Wang et al., 2021). Lake ice has a significant impact on the surface energy balance and can be an indicator of climate change (Walsh et al., 1998). Freezing of lake surface alters the physical environment of the water body, including light conditions and temperature

* Corresponding author. ORCID: 0000-0003-1313-6313. E-mail: qiuyb@aircas.ac.cn

that subsequently affects freshwater ecosystems in winter (Lindenschmidt et al., 2018). In many lakes, melting of ice in spring can be associated with significant methane emissions (Wang et al., 2023). Transportation, fishery, and recreation in the boreal and Arctic regions also depend on the quality of lake ice cover. Therefore, accurate lake ice parameters are needed in many applications.

Lake ice data are mainly derived from in situ observations and remote sensing satellites. Compared to Europe and North America, the record of lake ice observations in Asia is very limited (Newton and Mullan, 2021). In situ observations are concentrated in easily accessible lakeshore areas, which may not comprehensively represent the overall ice conditions, and researchers turn to use remote sensing observations. Passive microwave remote sensing has the unique advantage of penetrating freshwater ice and being unaffected by clouds and darkness. Due to an order of magnitude difference between the effective permittivity of water and ice (Rees, 2005), microwave brightness temperature (TB) is sensitive to the phase of the lake surface, and therefore TB is widely used to monitor lake ice and other components of the cryosphere including sea ice, snow, and river ice (Cai et al., 2022; Du et al., 2017; Kang et al., 2010, 2014; Wang et al., 2022).

The microstructure of lake ice results from thermodynamic processes and is an important characteristic affecting microwave radiation transfer in the ice. The physical temperature of ice is determined by heat transfer and the boundary conditions at the atmosphere-snow/ice and ice-water interfaces (Leppäranta, 2023), which affects the effective microwave temperature (Tonboe et al., 2011). Lake ice consists of ice crystals, gas bubbles, and some other impurities, and uneven ice growth can result in rough ice-water or ice-snow interfaces. When slush on the ice surface freezes to form snow-ice, this process results in high gas bubble content which affects microwave scattering and emission. When liquid water freezes to form congelation ice, dissolved gases are retained between ice crystals in the form of bubbles (Michel and Ramseier, 1971; Warren, 2019). These gas bubbles can result in slow ice growth directly below creating water-filled and uneven areas. Therefore, gas bubbles in ice are an important factor affecting lake ice roughness and microwave radiation transfer (Engram et al., 2013). Remote sensing provides a daily instantaneous characterization of lake ice cover, which does not capture higher resolution processes of lake ice formation and ablation as well as structural changes. Numerical models can help to understand the evolution of lake ice and its microwave radiation transfer (Cheng et al., 2014; Kontu et al., 2014; Picard et al., 2018; Yang et al., 2021).

Ice phenology and properties depend on local climate and lake characteristics (Leppäranta, 2023). Ice grows interactively with snow accumulation, and some models incorporate a snow layer on the top of the ice so that thermodynamic modeling can be based on mass and energy balance (Leppäranta and Wang, 2008). One-dimensional thermodynamic models that take snow into account can effectively enhance the simulation accuracy (Semmler et al., 2012; Yang et al., 2021). In typical full thermodynamic models, such as the Canadian Lake Ice Model (CLIMo) and the one-dimensional high-resolution thermodynamic snow and ice (HIGHTSI) models, the output parameters are ice thickness, snow depth, and temperature distribution of the snow and ice interior at a daily/hourly time step and any number of layers (Brown and Duguay, 2011; Cheng B et al., 2014; Cheng Y B et al., 2020; Duguay et al., 2003; Launiainen and Cheng, 1998; Ménard et al., 2002; Yang et al., 2012). These models have found extensive use in the numerical modeling of snow and ice parameters in the Arctic and subarctic regions, thereby improving our standing of these complex environments. As remote sensing technology has improved, the correlation between the thermal and electromagnetic properties of ice has gradually gained more attention. One-dimensional thermodynamic ice models combined with surface temperature derived from passive microwave or thermal infrared remote sensing data can determine the thermodynamic growth rate of ice, which has been used to improve the precision of ice thickness estimation in the Arctic and subarctic regions or to estimate ice growth in these cold regions from a spatial perspective (Anheuser et al., 2023; Karvonen et al., 2017; Kheyrollah Pour et al., 2017). The statistical relation between lake ice thickness and the space-borne TB data based on the forward results of a microwave radiation transfer model has been used to retrieve ice thickness in the subarctic lakes (Kang et al., 2014). Combinations of thermodynamic and microwave radiation transfer models can be employed to understand the emission and scattering of snow and ice and to provide a priori variables for the inversion of snow and ice properties from passive microwave data.

Microwave radiation transfer models such as the Helsinki University of Technology Snow Emission Model, the Microwave Emission Model of Layered Snowpacks, and the multilayer active-passive Snow Microwave Radiative Transfer Model (SMRT) are designed to simulate microwave thermal emission and backscatter in snow and ice parameters (including snow, sea ice, and freshwater ice) in the polar related regions by using the physical parameters of snow and ice including ice thickness, ice temperature, snow depth, and snow temperature as inputs (Picard et al., 2018; Vargel et al., 2020). Most studies on the combination of thermodynamic and microwave radiation transfer models have focused on snow cover, explaining the variation of snow properties or improving the algorithm of snow water equivalent inversion (Fuller et al., 2015; Kontu et al., 2017; Larue et al., 2018; Pan et al., 2011; Rostosky et al., 2020). Modeling studies of sea ice focused on the simulation of thermal emission from ice. By coupling a one-dimensional snow-covered sea ice thermodynamic model with a microwave emission model, the microwave emission process from sea ice could be simulated to understand the relationship between the physical temperature and TB

(Burgard et al., 2020; Tonboe, 2010; Tonboe et al., 2011; Willmes et al., 2014). There are fewer studies on the combination of lake ice modeling. Some of them have applied a lake ice thermodynamic model and a microwave radiation transfer model to consider the influence of lake ice physical properties on different microwave signals, specifically in the high Arctic region of Canada, focusing on the backscatter dependence on roughness and gas bubbles (Dabboor and Shokr, 2021; Murfitt et al., 2022, 2023). However, there has been little attention given to how lake ice properties (gas bubbles, ice thickness, and ice temperature) affect its TB. Therefore, this study proposes a combination of a thermodynamic model and a microwave radiation transfer model to investigate the effects of lake ice properties on TB in a Pan-Eurasian Experiment (PEEX) domain, Hulun Lake. The PEEX program founded by European, Russian, and Chinese research institutes focuses on the environment of Northern Eurasia, particularly the Arctic and subarctic regions.

Hulun Lake in Inner Mongolia Autonomous Region is the northernmost large lake in China, with a continental climate similar to Siberia. It experiences long, harsh winters and short, cool summers, and is rich in forest and wetland ecosystems. Hulun Lake undergoes long periods of ice cover with the duration over six months each year and the average maximum ice thickness exceeding 1 m. Similar climate conditions, ecological environments, and prolonged ice cover make the freeze-thaw process of Hulun Lake comparable to lakes in the subarctic. Therefore, this study takes Hulun Lake as a typical domain for studying the thermodynamic and microwave radiative process of lake ice in the subarctic region.

This study utilized the HIGHTSI (Cheng et al., 2014; Launiainen and Cheng 1998; Yang et al., 2012) to simulate the thermodynamics of snow and ice in Hulun Lake, and to use the output parameters as inputs to the SMRT (Picard et al., 2018). The feasibility of these models to simulate the TB of the lake ice was explored. The simulated TB was compared with the observations of the space-borne passive microwave radiometer. Subsequently, the thermal evolution and TB of Hulun Lake ice cover were analyzed.

2 Method and materials

2.1 Study area

Hulun Lake (48°31′N–49°20′N, 116°58′E–117°48′E) is located in the Hulun Buir Steppe close to the border of China, Mongolia, and Russia. The average water area of Hulun Lake is ~2169 km^2 (Bao et al., 2021). In the ice periods of 2002–2010, the annual mean winter air temperature and wind speed were approximately −4.2 ℃ and 3.3 m·s^{-1}, respectively. The average of minimum air temperature and maximum wind speed were −28.6 ℃ and 8.7 m·s^{-1}, respectively. The meteorological parameters for simulation and the spaceborne TB data for comparison were extracted from the center point of Hulun Lake (48°56′N, 117°23′E), eliminating the possible effect of land (Figure 1).
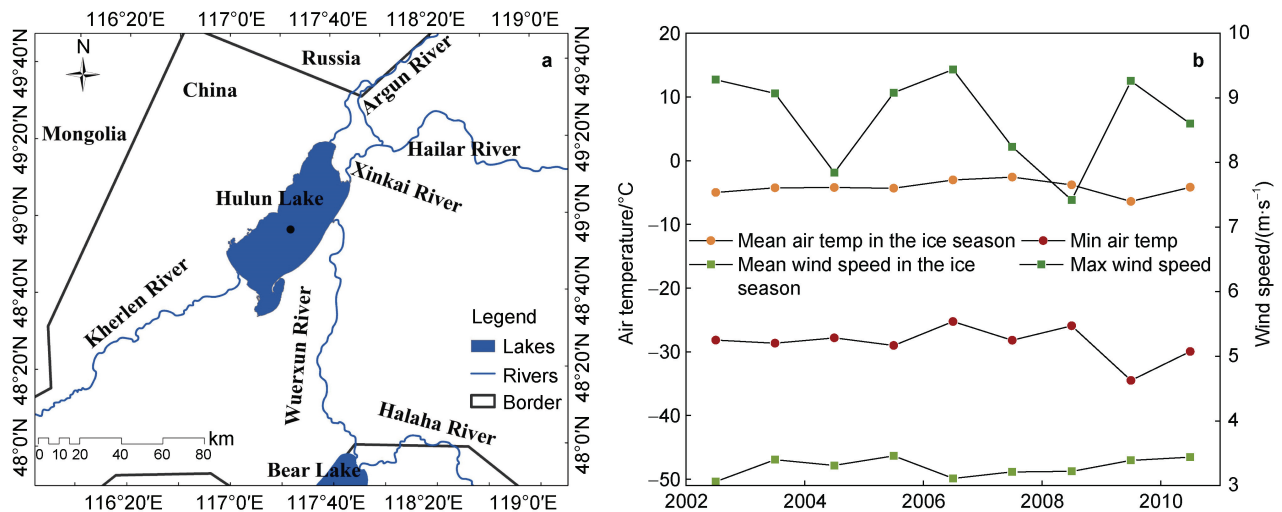

Figure 1 The location (**a**) and climate conditions (**b**) of Hulun Lake, China.

2.2 Data

2.2.1 Forcing data of HIGHTSI

The thermodynamic model was primarily driven by meteorological data sourced from the China Meteorological Forcing Dataset (CMFD) (He et al., 2020), including wind speed (at 10 m height), air temperature (at 2 m height), precipitation, downward shortwave radiation flux, downward longwave radiation flux, and humidity (available at https://doi.org/10.6084/m9.figshare.c.4557599). This dataset has a temporal resolution of 3 h and a spatial resolution of 0.1°×0.1°. It has been widely used in hydrological and climatological simulations. However, due to the absence of albedo and cloud cover data in the CMFD dataset, this study also utilized surface albedo data from the ERA5_land dataset provided by the European Centre for Medium-

Range Weather Forecasts (ECMWF) (available at https://cds.climate.copernicus.eu) and cloudiness data from the ERA5 dataset (with a temporal resolution of 1 h and spatial resolution of 0.25°×0.25°). All parameters were linearly interpolated to a 1-h time step to serve as forcing data.

2.2.2 Calibrated Enhanced-Resolution Passive Microwave Daily EASE-Grid 2.0 (CETB) brightness temperature and lake ice thickness data

The simulated TB was validated using CETB data. CETB is used for monitoring cryospheric and hydrological time series, covering the period from 1978 to present (Brodzik et al., 2016). This dataset aims to maximize the spatial resolution while maintaining low noise levels, ranging from 3.125 km to 25 km (Long et al., 2019). CETB incorporates space-borne TB data from three different sensors at different periods. Among these sensors, the data from the Advanced Microwave Scanning Radiometer for EOS (AMSR-E) has the highest spatial resolution at the frequency of 18.7 GHz. Thus, for this study, the space-borne TB data at the frequency of 18.7 GHz were selected from AMSR-E during the period from June 2002 to November 2011, with a spatial resolution of 6.25 km×6.25 km (Kawanishi et al., 2003).

Due to the lack of in situ observations of lake ice thickness, this study used a dataset for lake ice from 16 large lakes in the Northern Hemisphere based on radar altimetry satellite echo returns (Li et al., 2022; https://doi.org/10.5281/zenodo.5528542) to validate the simulated ice thickness in the Hulun Lake. This dataset employs a dual-threshold tracking algorithm to detect signals from the ice bottom and ice surface in radar echo waveforms, calculates the time interval between the two signals, and inversely derives the lake ice thickness based on the microwave propagation velocity within the ice, with an accuracy of approximately 0.2 m. Furthermore, ice phenology data for Hulun Lake based on optical remote sensing retrieval (Wu et al., 2019) was employed to verify the ice phenology obtained from the simulated ice thickness.

2.3 Model

2.3.1 HIGHTSI

The HIGHTSI is a one-dimensional model that considers heat transfer in a vertical multi-layer system. Originally applied for sea ice, it is currently widely utilized in the thermodynamic modeling of lake ice (Cheng et al., 2006, 2014; Launiainen and Cheng, 1998; Semmler et al., 2012; Yang et al., 2012). The model simulates the formation and melting of lake ice and ice temperature based on thermal conduction and sunlight transfer within ice and the boundary conditions forced by meteorological data.

2.3.2 SMRT

The SMRT is utilized for solving active and passive microwave radiation energy transfer within the range of 1–200 GHz in multi-layered snow/ice cover (Picard et al., 2018). The input parameters are for each layer temperature, thickness, density, and microstructure. Even though SMRT is primarily designed for snow study, restrictions on materials are not made explicit, thereby permitting adaptations to other media (ice, soil and atmosphere). Assuming that the medium is horizontally uniform, SMRT is a mature model which can be configured with different medium and electromagnetic radiation models. Due to its flexible configuration, SMRT has been applied to investigate Arctic and subarctic snow emission, ice brightness temperature, and ice backscatter (Fan et al., 2023; Murfitt et al., 2022, 2023, 2024; Vargel et al., 2020). By specifying the microwave frequency, incidence angle, and polarization, the model eventually returns the radiation intensity of snow/ice at the given frequency, polarization, or for specific directions.

2.4 Combining of the HIGHTSI and SMRT

A combined model named HiGHTSI-MRT has been developed, integrating a one-dimensional thermodynamic model with a microwave radiation transfer model (Figure 2). The HIGHTSI model was driven by meteorological data with a temporal resolution of 1 h, producing the thermal evolution of ice and snow. The outcome, including lake ice thickness, snow depth, and the temperature profile in ice and snow, were transformed into input parameters for the SMRT through layer-wise averaging, simulating the changes in the passive microwave radiation energy of lake ice.

The study used the wind speed, air temperature, precipitation, downward shortwave radiation flux, downward longwave radiation flux, and humidity data from CMFD to drive HIGHTSI in simulating the ice evolution process in Hulun Lake (48°56′N, 117°23′E) from 2002 to 2011. The CMFD for the Hulun Lake region served as the primary input data source. For the precipitation data, the type of precipitation was determined based on temperature thresholds (T_a<0.5 ℃) to distinguish between solid and liquid phases (Yang et al., 2012). Relative humidity was calculated using air temperature, pressure, and specific humidity data, and surface albedo data were obtained from the ERA5_land dataset, while cloudiness data for the extinction coefficient of ice were obtained from the ERA5 dataset.

The basic configuration of the HiGHTSI-MRT is presented in Table 1. In the HIGHTSI, the number of layers for both ice and snow was set to 20 for an accurate thermodynamic simulation. For the SMRT model, a conventional four-layer stratification setup was utilized. The Improved Born Approximation, the discrete ordinate and eigenvalue method, and Sticky Hard Spheres were employed as the electromagnetic radiation model, the radiation transfer equation solving method, and the microstructure model, respectively.
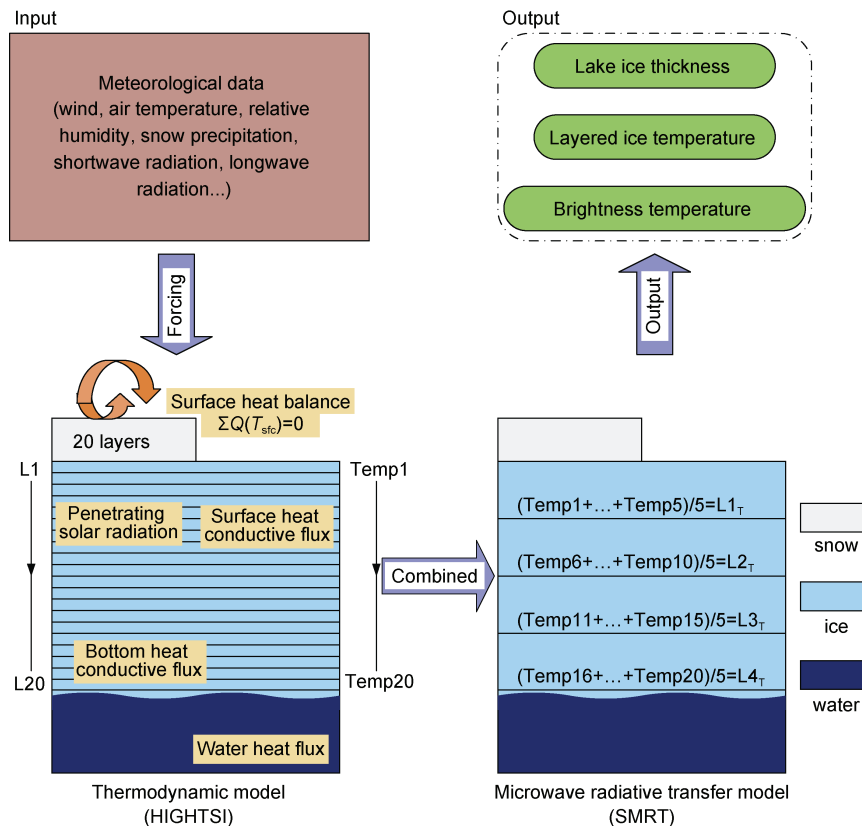
Figure 2 The combining strategy of thermodynamic and microwave radiation transfer model.

Table 1 HiGHTSI-MRT parameter settings

HIGHTSI		SMRT	
Initial ice thickness	5 cm	Ice porosity	1%
Initial snow depth	0 cm	Correlation length	5 mm
Ice bottom temperature	−0.8 ℃	Frequency	6.9–89.0 GHz
Initial ice surface albedo	0.75	Bubble radius	0–3 mm (interval value is 0.25 mm)
Initial snow surface albedo	0.85	Salinity	0 or 1‰
Layers	20	Layers	4

3 Results and comparison

3.1 HiGHTSI-MRT simulation

3.1.1 The process of lake ice evolution

Figure 3 shows the evolution of ice and snow cover from 2002 to 2011 in Hulun Lake. The vertical temperature characteristics were as follows: the temperature of snow layers increased from top to bottom, with the surface temperature close to the air temperature and lower than the temperature at the snow-ice interface. Similarly, the temperature of lake ice increased from top to bottom. Over the whole time series, ice and snow temperatures decreased initially and then increased, reaching their minima before the date of maximum ice thickness, and reaching their maximum in the melting stage.

The simulations began on 1 October each year with an initial ice thickness of 5 cm. If the weather conditions were not favorable for ice growth, the model would reduce the ice thickness to 2 cm. The freezing date and melting date were defined as the first occurrence of five consecutive days with simulated ice thickness greater than 2 cm and less than 2 cm, respectively (Yang et al., 2012). The statistical results of lake ice phenology (Table 2) indicate that Hulun Lake freezes annually between late October and early November, and melts in the latter half of May, with an average ice period exceeding six months (204 d). The longest ice period was recorded in 2002–2003 (215 d), while the shortest one occurred in 2008–2009 (181 d). The time series of maximum ice thickness and snow depth from 2002 to 2011 is illustrated in Figure 4. The maximum ice thickness exhibited a decreasing trend, whereas the maximum snow depth showed a slight increase. The simulation results showed that the maximum ice thickness in the region was large, consistently exceeding 1 m, while the snow depth remained shallow, with an average maximum snow depth of approximately 8 cm.

3.1.2 The relationship between lake ice thickness and TB at different frequencies

Figure 5, taking 2002–2003 as a representative ice season, shows the correlation between bubble-free TB at various frequencies and ice thickness in 2002–2003. Figure 5
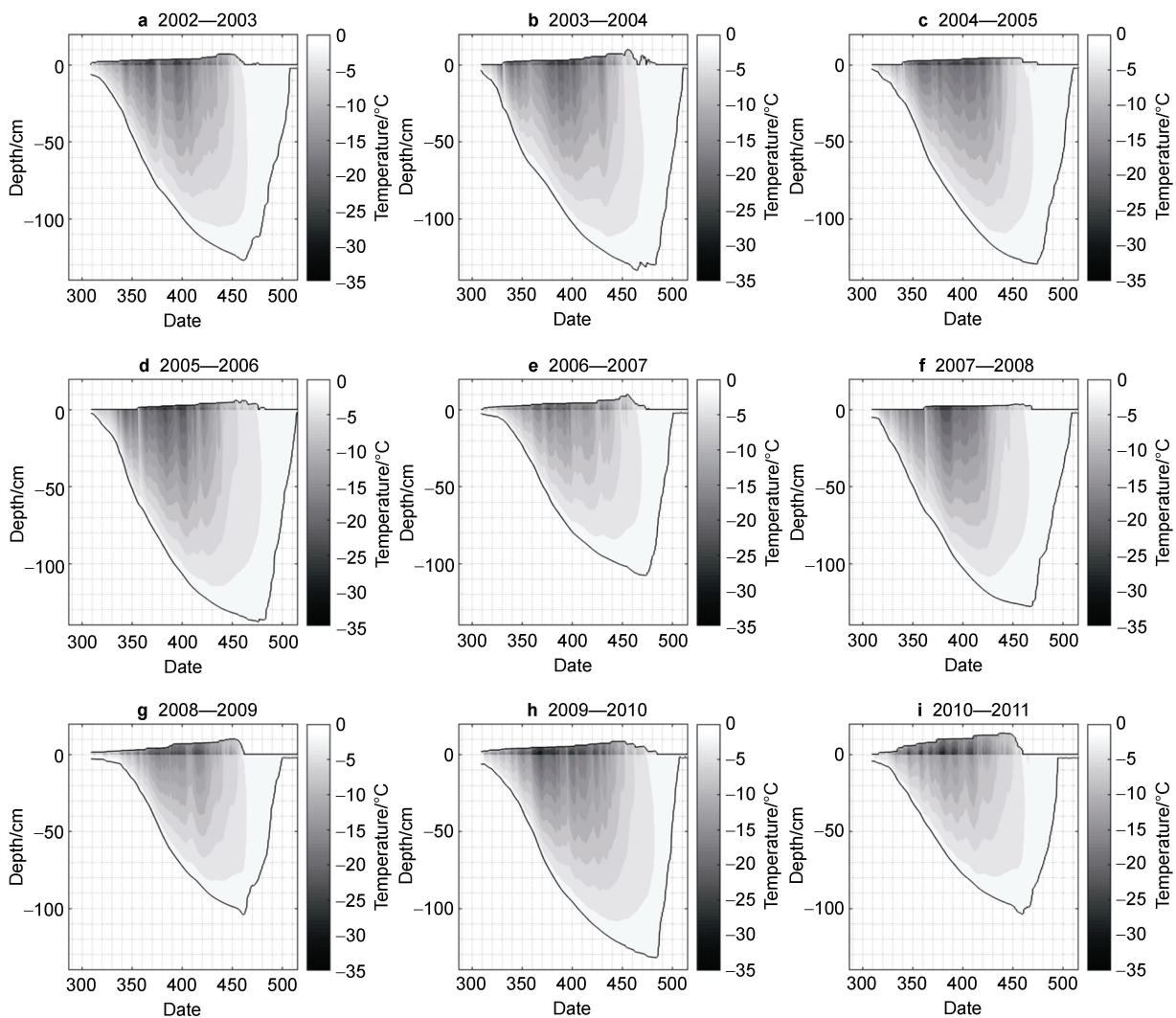
Figure 3   Thermal evolution of snow and ice in Hulun Lake simulated from HiGHTSI-MRT model.

Table 2   Lake ice phenology in Hulun Lake simulated from HiGHTSI-MRT model

Year	Freezing date	Melting date (next year)	Ice period/d
2002	20 Oct. (day 293)	23 May (day 508)	215
2003	1 Nov. (day 305)	24 May (day 510)	205
2004	23 Oct. (day 297)	24 May (day 510)	213
2005	5 Nov. (day 309)	29 May (day 514)	205
2006	5 Nov. (day 309)	16 May (day 501)	192
2007	26 Oct. (day 299)	23 May (day 509)	210
2008	14 Nov. (day 319)	14 May (day 500)	181
2009	28 Oct. (day 301)	22 May (day 507)	206
2010	14 Oct. (day 287)	10 May (day 495)	208

shows that at six frequencies TB increases with increasing ice thickness, regardless of polarization. After the high-frequency TB had reached saturation at a certain depth, the change in ice thickness no longer affected TB. This reflected how passive microwave radiation in different frequencies penetrated lake ice. For example, the maximum value of TB at 89.0 GHz reached at 10–20 cm of lake ice, while TB at 36.5 GHz reached its maximum value at about 1 m thickness. Thereafter, TB remained constant with increasing ice thickness. The correlation between ice thickness and TB decreased as the frequency increased, and TB was slightly higher at vertical polarization (V-pol) than at horizontal polarization (H-pol). As shown in Table 3, TB at 6.9–18.7 GHz is significantly correlated with ice thickness ($R^2 \geqslant 0.98$). Comparing the slopes of the regression lines, the sensitivity of TB to ice thickness increased with frequency, with TB the most sensitive at 18.7 GHz. The correlation of TB with ice thickness decreased remarkably ($0.382 \leqslant R^2 \leqslant 0.961$) as the frequency increased within 23.8–89.0 GHz. When the ice thickness was less than 10 cm, the higher the frequency, the more sensitive TB was to ice thickness, and TB at 89.0 GHz was the most sensitive. When the ice thickness exceeded 10 cm, the overall performance of TB was better at low frequency than at high frequency, while 23.8 GHz was susceptible to moisture.
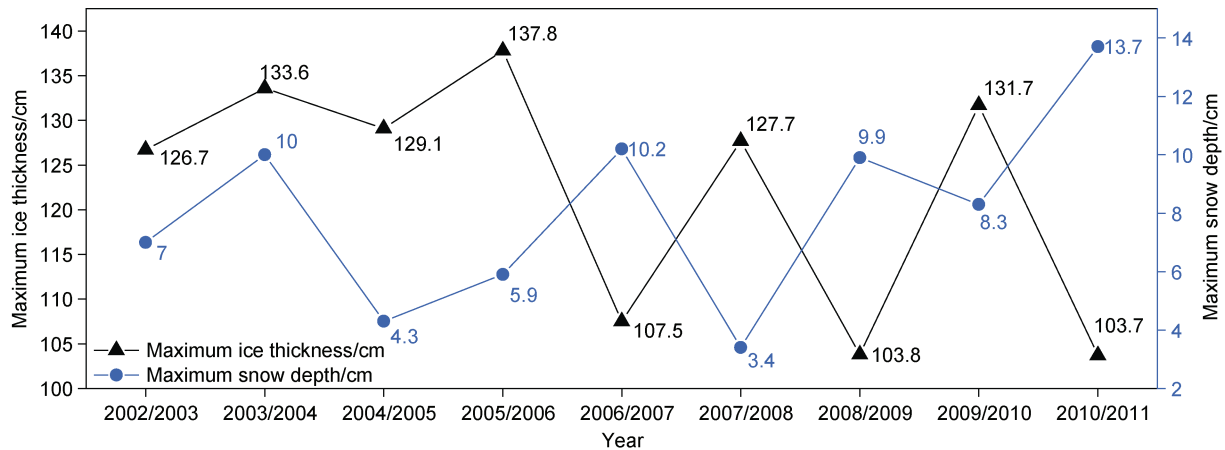
Figure 4   The maximum ice thickness and snow depth during 2002−2011 in Hulun Lake simulated from HiGHTSI-MRT model.
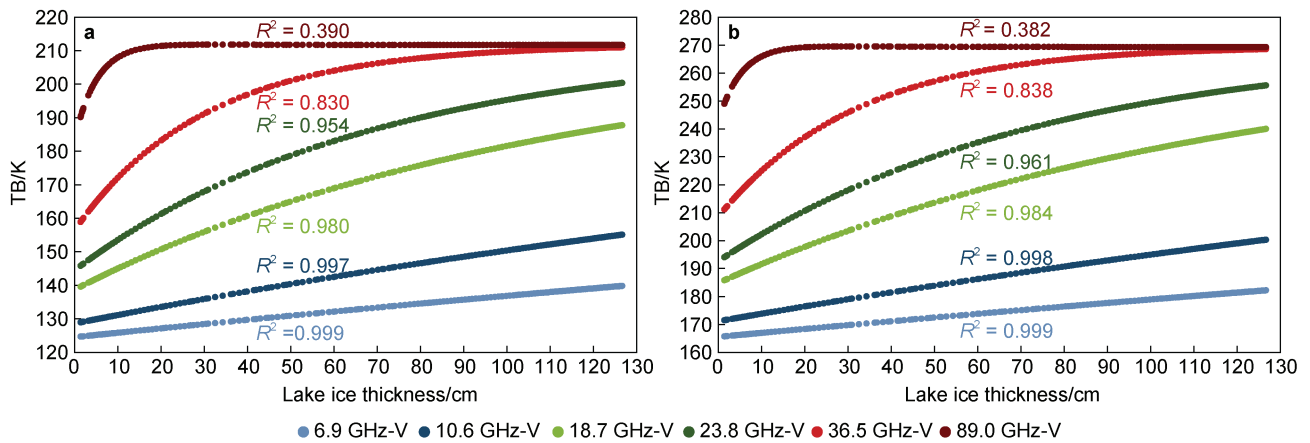

Figure 5   The relationship between TB and lake ice thickness. **a**, TB at H-pol; **b**, TB at V-pol.

Table 3   Parameters for the linear fit of TB (V-pol and H-pol) to lake ice thickness

	6.9 GHz		10.6 GHz		18.7 GHz	
	H	V	H	V	H	V
Slope	0.12	0.13	0.21	0.23	0.38	0.43
Intercept	124.7	165.7	129.3	171.8	142.8	188.9
R^2	0.999	0.999	0.997	0.998	0.980	0.984

	23.8 GHz		36.5 GHz		89.0 GHz	
	H	V	H	V	H	V
Slope	0.42	0.42	0.37	0.41	0.08	0.07
Intercept	151.4	200.3	172.3	225.3	204.0	262.1
R^2	0.954	0.961	0.830	0.838	0.390	0.382

Therefore, for the inversion of thin ice, high frequency, such as 89.0 GHz, TB was suitable, while for the retrieval of thick ice, TB at low frequencies, such as 6.9 GHz, was appropriate (Burgard et al., 2020; Surdyk, 2002). In terms of the sensitivity of TB at different frequencies to snow and ice thickness, 18.7 GHz V-pol was suitable for ice thickness because it was not affected by a small amount of snow on the ice and responded relatively quickly to changes in ice thickness.

3.1.3   The effect of snow and bubbles on TB at 18.7 GHz

Figure 6 illustrates the simulated TB at 18.7 GHz under different conditions. A comparison is made between the TBs in V-pol and H-pol at 18.7 GHz under snow-covered and snow-free conditions in Figure 6a. The results indicate that the simulated TB at V-pol consistently exceeds that at H-pol. The average absolute deviation of TBs at V-pol and H-pol was 50 K for snow-free conditions and 31 K for snow-covered conditions. The simulated TB at 18.7 GHz V-pol was not significantly affected by snow. The simulated TBs at 18.7 GHz V-pol under snow-free and snow-covered conditions had an absolute deviation less than 1 K. Hence, TB at 18.7 GHz V-pol is more suitable for investigating the response of lake ice to passive microwave radiation. A similar result was observed by resetting the snow depth to 10 times the original data or by comparing the relationship between simulated TB at different frequencies and ice thickness, as discussed in Section 3.1.2.

When gas bubbles of different sizes are present in the ice, variations occur in TB at 18.7 GHz V-pol (Figure 6b). The simulated TB time series consistently exhibited an
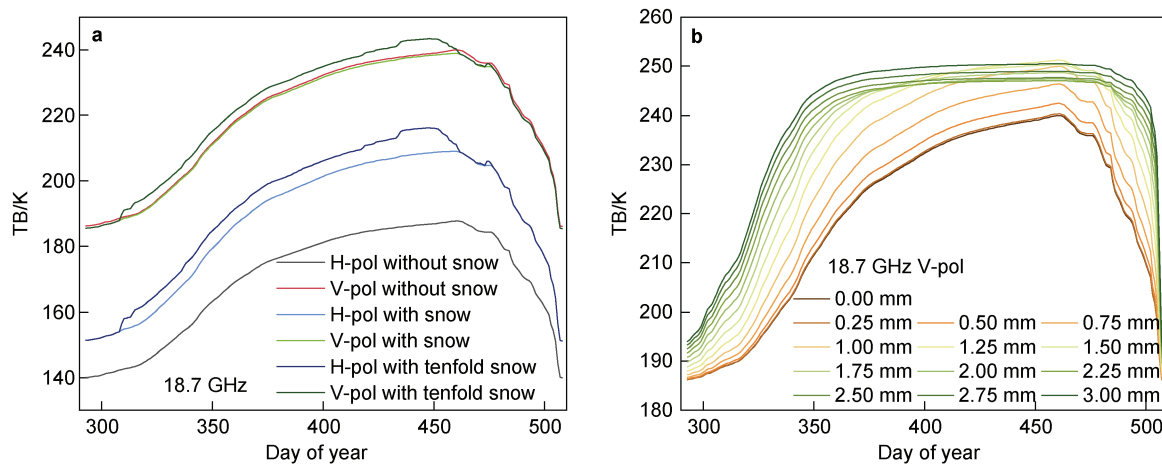
Figure 6 Simulated TB at 18.7 GHz (V-pol and H-pol) without bubbles (**a**), and simulated TB at 18.7 GHz V-pol with bubbles (**b**) during 2002–2003.

initial increase followed by a decrease, regardless of the presence of bubbles in the ice. During the increasing stage, larger bubbles led to an earlier attainment of the maximum TB, and then TB remained relatively stable at a high level for a long duration. Thus, during the cold season, when the radius of the bubbles fell between 0–1.25 mm, the simulated TB curve closely resembled an inverted "V" shape. For bubble radius ranging from 1.25 to 3 mm, the shape was that of an inverted "U". During the rapid stages of change, TB consistently increased with the increasing bubble radius. However, in midwinter, when the bubble radius ranged from 1.5 to 2.25 mm, TB at 18.7 GHz V-pol decreased with the increasing bubble radius. Conversely, when the bubble radius ranged from 0 to 1.5 mm or from 2.5 to 3 mm, the simulated TB increased with the increasing bubble radius.

3.2 Comparison of the simulation

The simulation of the HiGHTSI-MRT combined model was in good agreement with the physical evolution and microwave radiation transfer in lake ice. To further assess the simulation performance, we compared CETB at 18.7 GHz V-pol from the center point of Hulun Lake with simulated TB at the same frequency under snow-free conditions and adjusted the HiGHTSI-MRT parameters to optimize the model. By varying the bubble size, the influence of lake ice microstructure on TB was studied. The bubble size was controlled by the bubble radius ranging from 0 to 3 mm at intervals of 0.25 mm. To account for the inter-annual variation in salinity in Hulun Lake (Guo et al., 2022), experiments were conducted by setting the bubble radius to 1.25 mm and the salinity to 1‰ for certain years.

3.2.1 Comparison of simulated and observed lake ice information

The accuracy of simulated lake ice was validated by using the lake ice parameters retrieved from remote sensing

data due to the lack of in situ data. First, the daily mean ice thickness simulated for the Hulun Lake from 2002 to 2011 was compared with the lake ice thickness retrieved by altimetry satellites using radar echoes (Li et al., 2022) (Figure 7 and Table S1). The results showed that the modeled ice thickness was generally consistent with the remotely sensed ice thickness (R^2= 0.74) and yielded a high temporal resolution (hourly) of lake ice evolution. The ice phenology data were obtained based on the simulated ice thickness as shown in Table 2. When comparing the simulation with the result from optical remote sensing (Wu et al., 2019) (Table 4), the modeled freezing date had an average bias of 6.5 d, and the melting date had an average bias of 8 d. The simulated freezing date tended to occur later than the remotely sensed date, which may be due to the influence of strong winter winds in the region. Given the various definitions of phenology and the fact that the combined model was based on a one-dimensional model, the deviation in phenology was considered acceptable.
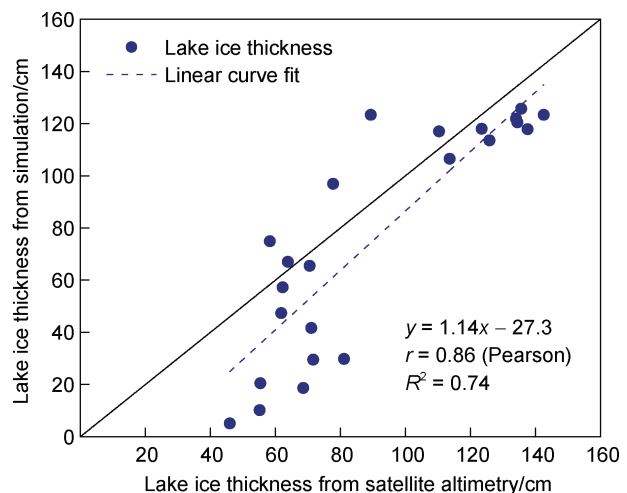

Figure 7 Comparison of simulated and satellite altimetry ice thickness in Hulun Lake during 2002–2011.

Table 4 Comparison of simulated and remote sensing lake ice phenology (day of year)

Year	Freezing date from remote sensing data	Freezing date from simulation	Melt date from remote sensing data	Melt date from simulation
2002	Day 299	Day 293	Day 501	Day 508
2005	Day 303	Day 309	Day 497	Day 514
2008	Day 305	Day 319	Day 495	Day 500
2010	Day 287	Day 287	Day 492	Day 495

3.2.2 Comparison of simulated and observed brightness temperatures

Figure 8 shows the comparison between simulated and observed TB. Differences in the winters of 2002–2006 and 2007–2008 were primarily as follows: the simulated TB initially increased as the lake froze over, reached a peak and remained stable for a period, and then rapidly decreased upon ice melting, with variations depending on the gas bubbles. In contrast, the observed TB first experienced a sudden increase, followed by a weak decrease and slow increase, and finally TB had a sharp peak before a rapid decline within a short time. Combined with Figure 9 and Table S2, it's obvious that setting the bubble radius to 1 mm yielded the best performance during the ice seasons of 2002–2003 and 2003–2004, with RMSE values of 16.4 K and 16.2 K, respectively. The next best simulation with the same bubble radius occurred in 2004–2005 and 2007–2008, with RMSE values of 21.2 K and 26.3 K, respectively. In the winters of 2006–2007 and 2008–2011, the observed TB experienced a sudden change upon freezing, maintaining a

high value until the ice breakup. This may be influenced by ice salinity. The simulation performance was at its poorest in 2008–2009, with the optimal bubble radius being 2.75 mm and an RMSE of 67.3 K. The performance reached its peak in the four winters in 2005–2007 and 2009–2011 when the bubble radius was set to 3 mm, with RMSE values of 23.5 K, 26.6 K, 24.8 K, and 27.9 K, respectively. Hence, the size of bubbles had an impact on the accuracy of TB simulation.

With the segmentation of lake ice season to stages outlined in Section 4.1, we compare the simulation performance of TB in different periods (Figure 9 and Table S2). The RMSE was smaller during the stable ice growth period than in the other two periods for the vast majority of years. Only 2008–2009 showed a smaller RMSE during the ablation period compared to the growth and slow growth periods (defined in Section 4.1). When the bubble radius was set to 1 mm, the performance was best in the slow growth period of the three winters from 2002 to 2005, with RMSE values of 7.9 K, 8.0 K, and 8.9 K, respectively. Similarly, when the bubble radius was set to 1.25 mm, the simulation performance was best during the slow growth period of winters from 2005–2006 and 2007–2008, with RMSE values of 7.5 K and 10.4 K, respectively. During the slow growth period of winter 2006–2007 and two winters from 2009 to 2011, the performance was best when the bubble radius was set to 1.25 mm and salinity was set to 1‰. The RMSE values were 7.1 K, 4.6 K, and 9.1 K, respectively.

Overall, the simulation results are generally aligned with the actual conditions. They performed best in the slow
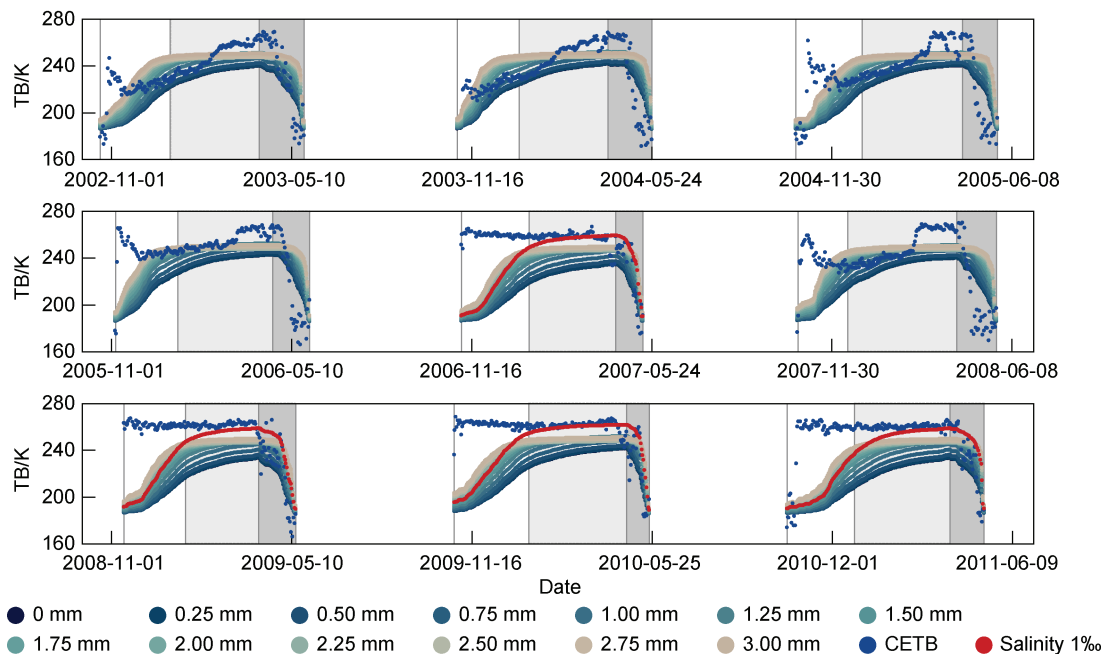

Figure 8 Comparison of simulated TB and CETB at 18.7 GHz V-pol in Hulun Lake. The rectangles are color-coded to represent different periods: white for growth, light gray for slow growth, and gray for ablation period.
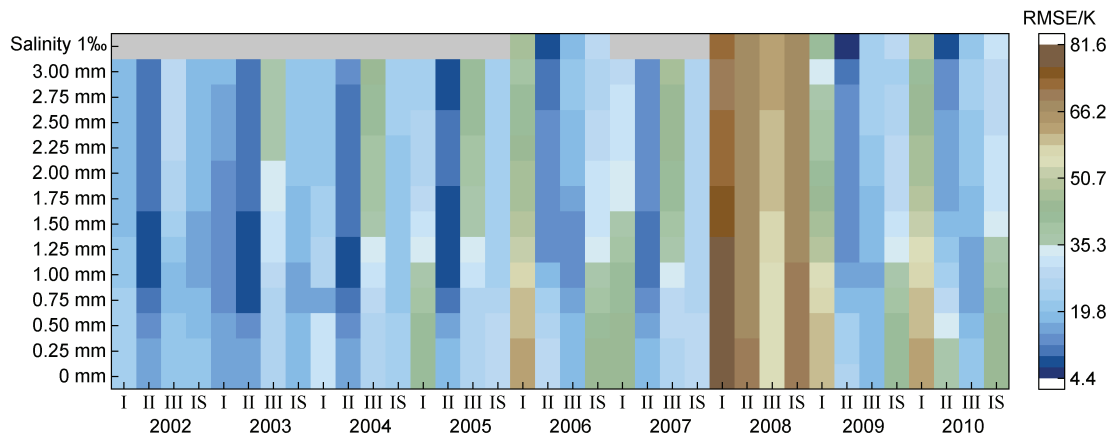
Figure 9 RMSE of simulated TB and CETB from 2002 to 2011. I, the growth period; II, the slow growth period; III, the ablation period; IS, the ice season.

growth period, followed by the growth period, and the performance was worst in the ablation period. Simulation errors primarily occurred in the early stages of the growth period and the later stages of the ablation period. In the parameter tuning, the size of bubbles and ice salinity had significant impacts. Subsequently, using the year 2002–2003 as a representative ice season, we conducted a detailed analysis of the evolution of lake ice and its relationship with TB, particularly focusing on its relation to TB at 18.7 GHz V-pol under no snow conditions.

4   Analysis based on HiGHTSI-MRT

4.1   Stages of lake ice development

The evolution of lake ice was divided into three phases based on ice thickness and lake-air temperature difference: the growth period, the slow growth period, and the ablation period. The growth period starts from the freezing date. By defining the date when the fit line of lake-air temperature difference crosses the zero point as the date when the lake ice growth rate starts to decrease, we have the end date of growth period. During this period, the air temperature is lower than the ice surface temperature. Additionally, the temperature continues to fall while lake ice grows rapidly. During the slow growth period, the rate of lake ice growth slows down until lake ice thickness reaches its maximum. At this stage, the air temperature is slightly higher than the ice surface temperature, and both show an upward trend. The ablation period is characterized by rapid melting of ice after it has reached its maximum thickness. During this period, the air temperature is above 0 ℃, and the ice surface temperature is continuously approaching 0 ℃.

The evolution of lake ice under bubble-free conditions were simulated by the HiGHTSI-MRT model. Figure 10 shows the ice growth and ablation process with TB during 2002–2003. The growth period was from 20 December 2002 to 2 January 2003, followed by a slow growth period from 3 January 2003 to 6 April 2003, and finally the

ablation period occurred from 7 April 2003 to 23 May 2003. The growth period started when the simulated ice thickness reached 2 cm and the lake froze over. At that time, the air temperature was below 0 ℃, the lake-air temperature difference was above 0 ℃, and the lake lost heat to the atmosphere. The rapid growth of lake ice was accompanied by a corresponding increase in TB. The average growth rates of ice and TB were 0.90 cm·d^{-1} and 0.48 K·d^{-1}, respectively. On 2 January 2003, the ice thickness increased to about 60 cm. Although the temperature of air and ice surface remained below freezing point, the surface temperature was generally less than and the temperature. The lake lost heat slowly and the growth of lake ice entered 91 d of slow growth. The average growth rate of ice and TB were 0.61 cm·d^{-1} and 0.19 K·d^{-1}, respectively. On 6 April 2003, the ice thickness peaked at 126.7 cm when the air temperature rose to above 0 ℃ and continued to increase. The ice surface temperature kept close to 0 ℃, and therefore the air-ice temperature difference was solely determined by the air temperature. As a result, the ice absorbed heat and began to melt rapidly, reaching breakup in 47 d. The average melt rate was 2.65 cm·d^{-1}, while the air temperature decreased on average by 1.15 K·d^{-1}. During the ablation period the ice thickness and TB decreased rapidly. These changes occurred at a much faster rate than during the growth periods. Therefore, caution is needed for the retrieval of ice thickness in this period.

4.2   Dependence of ice thickness on air and ice temperature

Air temperature is the key factor controlling freezing of lake surface and ice growth in the fall and winter, and dominates the melting of ice in the spring. The ice surface temperature reflects the heat exchange between ice and air, as well as the heat transfer in the ice. The ice surface-air temperature difference indicates the magnitude and direction of heat transfer. The surface temperature and air temperature can be used to estimate the evolution of ice thickness to some extent.
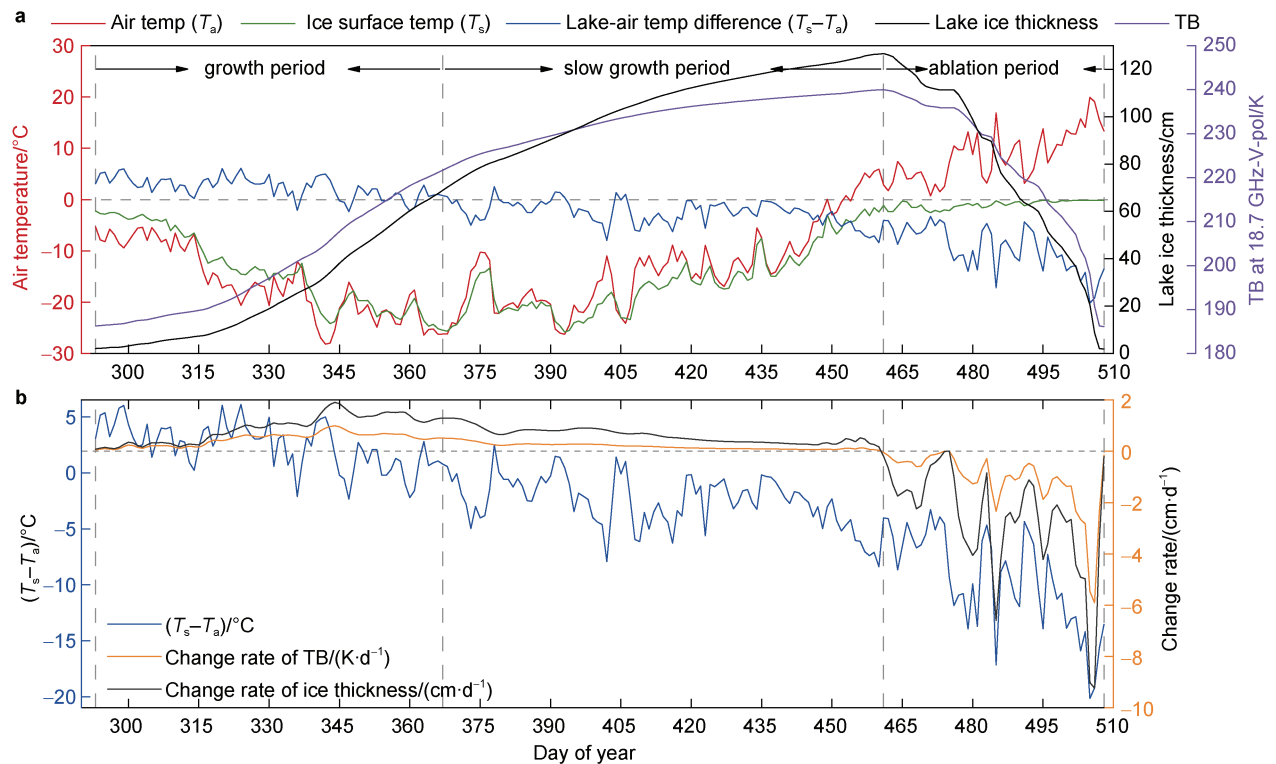
Figure 10 Time series of ice thickness, TB, air temperature, ice surface temperature (**a**), and the difference between lake and air temperature (**b**).

Table 5 displays the mean correlation coefficients between temperature parameters and both ice thickness and TB (pure ice) for the period 2002–2011, further illustrating the effect of the ice surface temperature on those variables. The results indicated that consistent correlations between the surface-air temperature difference and rates of changes in ice thickness and TB throughout the ice season (r=0.77 and r=0.78, respectively). The ice surface temperature plays a crucial role in the evolution of lake ice, with a particularly strong reflection of ice thickness during the growth period (r=−0.88). A similar pattern could be observed for TB. The strongest correlation between the ice surface temperature and TB occurred in the growth period (r=−0.90). However, the ice surface temperature effects on ice thickness were inconsistent at the other periods, exhibiting positive correlation during the slow growth period and negative correlation during the growth and ablation periods and, with the weakest effect occurring in the ablation period. During the ablation period, contributions of all temperature parameters to the change rates of ice thickness and TB are almost indistinguishable due to the ice surface temperature remaining at the melting point, hence lacking predictive power. The melting of ice is driven by the combination of rising air temperature and solar radiation. Table 5 also shows that the ice surface temperature is a good predictor for ice thickness and TB changes especially in the growth period (r=−0.87 and r=−0.74, respectively), but the ice surface temperature is coupled with air temperature so that

there is no simple functional relation (Leppäranta and Lewis, 2007). This can be demonstrated by the principle of the thermodynamic ice model. Actually, the upper boundary condition for the thermodynamic ice model is defined by the surface heat balance (Cheng et al., 2014). Once the ice surface temperature has been determined, the in-ice

Table 5 The mean correlation coefficients between temperature parameters and both lake ice thickness and TB during 2002–2011. I, the growth period; II, the slow growth period; III, the ablation period; IS, the ice season

Temp parameters		I	II	III	IS
Ice thickness	Air temp	−0.71	0.78	−0.59	0.09
	Ice surface temp	−0.88	0.79	−0.67	−0.07
	Lake-air temp difference	−0.27	−0.57	0.56	−0.33
Change rate of ice thickness	Air temp	−0.83	−0.74	−0.55	−0.79
	Ice surface temp	−0.87	−0.76	−0.57	−0.66
	Lake-air temp difference	0.06	0.48	0.55	0.77
TB	Air temp	−0.73	0.75	−0.59	0.05
	Ice surface temp	−0.90	0.76	−0.64	−0.13
	Lake-air temp difference	−0.26	−0.56	0.57	−0.32
Change rate of TB	Air temp	−0.76	−0.74	−0.59	−0.75
	Ice surface temp	−0.74	−0.75	−0.63	−0.60
	Lake-air temp difference	0.18	0.49	0.58	0.78

temperature profiles and ice thickness can be calculated based on the conservation of heat in ice. Several studies have utilized thermal infrared or passive microwave remote sensing data to acquire surface temperatures of ice, which in turn have been employed to estimate ice thickness (Kheyrollah Pour et al., 2017; Leppäranta and Lewis, 2007; Mäkynen et al., 2013; Similä et al., 2013; Singh et al., 2011; Wang et al., 2010). These results underscore the predictive role of ice surface temperatures, particularly during the growth period in which ice thickness is relatively thin. This suggested that the ice surface temperature can be used to estimate lake ice thickness, but different formulas are required in different stages of lake ice development, with the best results expected in the growing season.

Comparing the time series of ice thickness with TB of different frequencies and polarizations (pure ice) during 2002–2003 (Figure 11), the changing pattern of TB with ice thickness at other frequencies is similar to that of TB at 18.7 GHz. In terms of vertical stratification of the ice cover, ice temperature increased with increasing ice thickness, and the range of ice temperature decreased with increasing ice thickness. Table S3 shows correlation coefficients between ice temperature and TB of different frequencies (V-pol and H-pol). Figure 12 displays the correlation coefficients
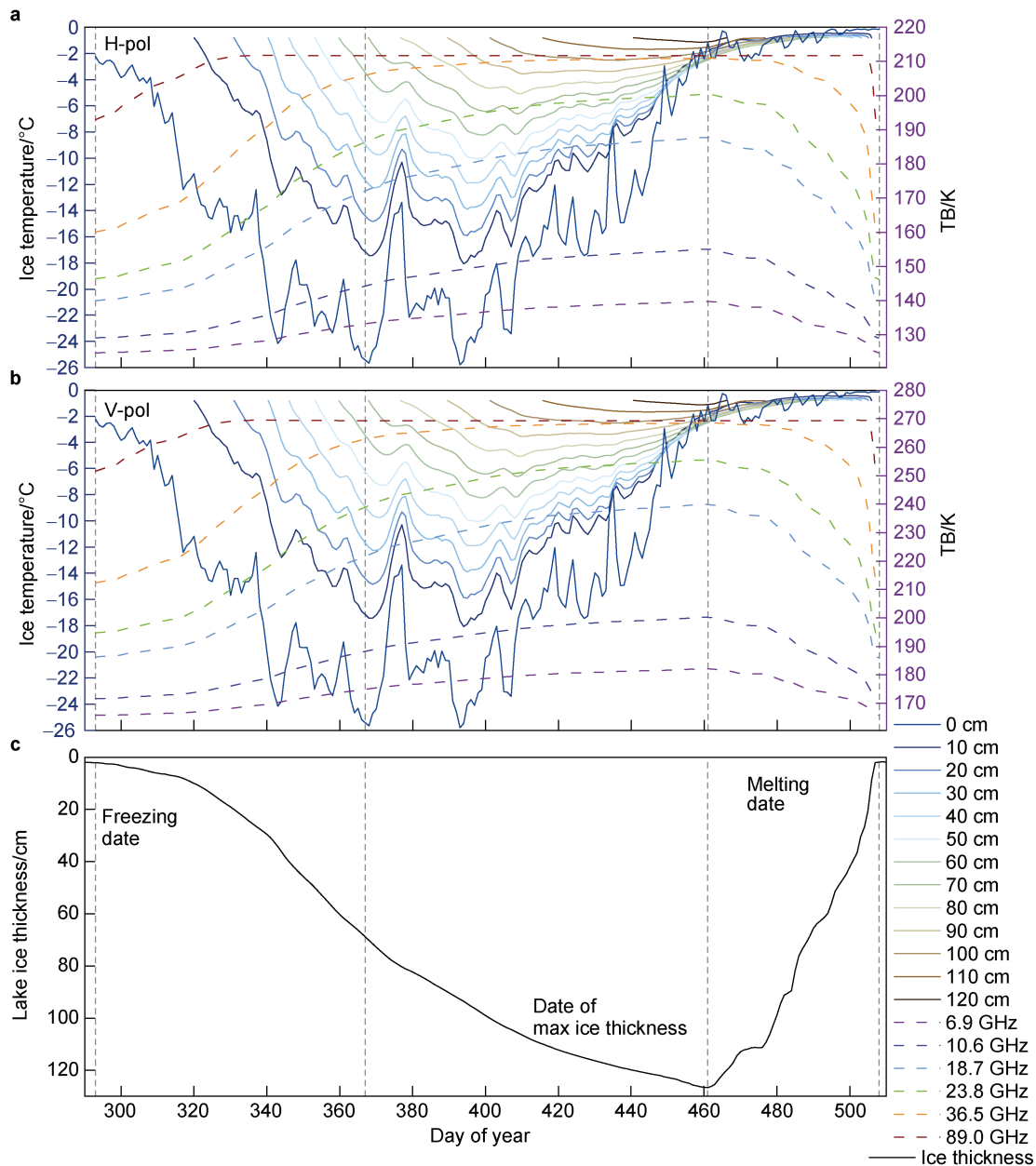
Figure 11 Time series of TB (dashed lines in **a**, TB at H-pol; dashed lines in **b**, TB at V-pol), lake ice thickness (**c**), and multilayer ice temperature (solid lines in **a**, TB at H-pol; solid lines in **b**, TB at V-pol) during the ice season 2002–2003.
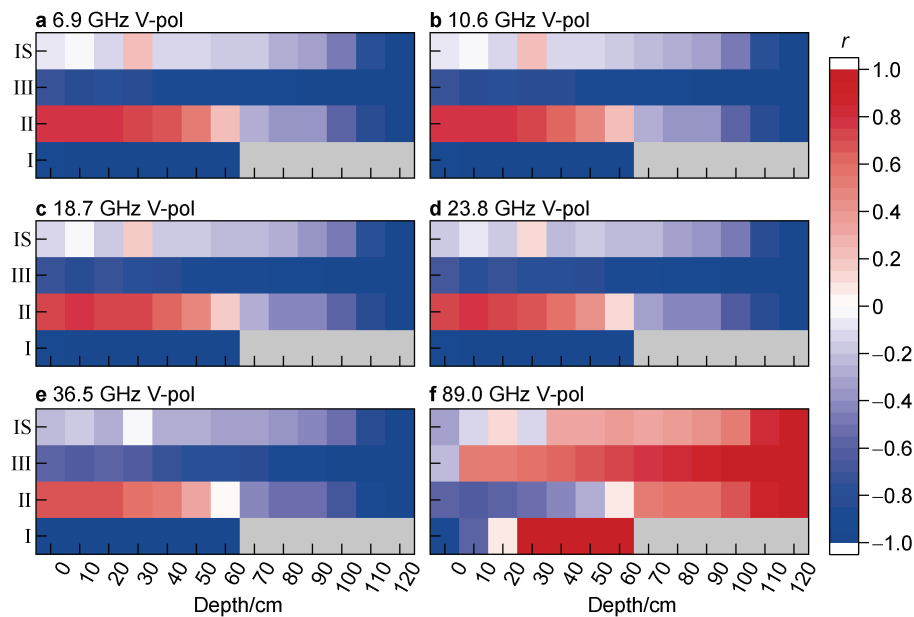
Figure 12 The correlation coefficients between ice temperature and TB during the ice season 2002–2003. I, the growth period; II, the slow growth period; III, the ablation period; IS, the ice season. **a**, 6.9 GHz V-pol; **b**, 10.6 GHz V-pol; **c**, 18.7 GHz V-pol; **d**, 23.8 GHz V-pol; **e**, 36.5 GHz V-pol; **f**, 89.0 GHz V-pol.

between ice temperature and V-pol TB at different periods. The distribution of the correlation coefficients is consistent except for TB at 89.0 GHz. Fluctuations in single-layer ice temperatures had little or no intuitive effect on TBs in the different frequencies and polarizations in the ice season. However, the relationship between ice temperature and TB was reflected in the different stages of ice evolution. Obviously, the correlation was strong during the growth period. During the slow growth period, TB correlated well with ice surface and bottom temperatures, although the trends were opposite. During the ablation period, the correlation between TB and ice temperature strengthened with depth.

In conclusion, TB is strongly related to both ice surface and internal temperatures at different stages of lake ice evolution, especially in the growth period. Given that the internal ice temperature is currently obtained by buoys, while the ice surface temperature can be obtained by various remote sensing data, the ice surface temperature is of great significance for the inversion of lake ice thickness.

4.3 Dependence of TB on ice thickness at different stages of ice development

The relationship between ice thickness and TB at 18.7 GHz V-pol for bubble-free conditions in different periods during 2002–2003 is shown in Figure 13. The trends of ice thickness and TB were positively correlated, i.e., higher TB corresponds to higher ice thickness. Table 6 compares the mean linear fitting parameters in different periods from 2002 to 2011. The results indicated that TB and ice thickness had a linear relationship in the growth period (slope is 1.81). The linear fit in the slow growth period was the best, with an R^2 close to 0.996. A quadratic polynomial fit of TB and ice thickness in different periods was generally better than the linear fit, with an average R^2 over 0.999, and the fit was best in the slow growth period. Therefore, it was anticipated that TB inversion for ice thickness would perform better with a quadratic rather than a linear polynomial.
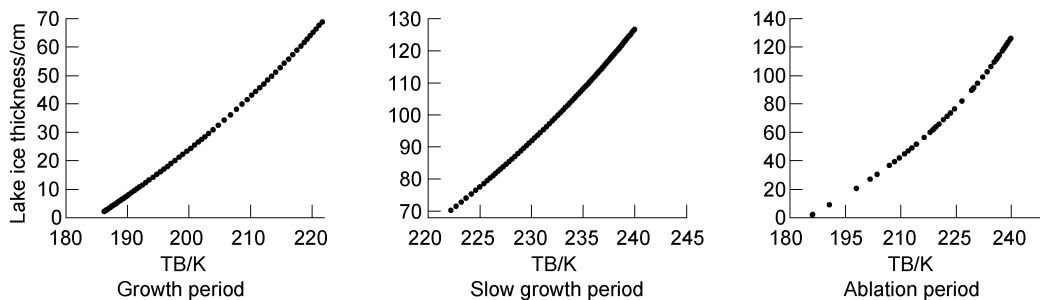
Figure 13 Scatterplot of bubble-free TB versus ice thickness for different periods in 2002–2003.

Table 6   Mean parameters fitted to TB and ice thickness for different periods during 2002–2011

Parameters	a	b	c	R^2
Formula		$H = bx + c$		
Growth period	\	1.81	−336.76	0.99592
Slow growth period	\	3.14	−628.86	0.99628
Ablation period	\	2.32	−441.11	0.98158
Formula		$H = ax^2 + bx + c$		
Growth period	0.01	−3.75	223.50	0.99997
Slow growth period	0.04	−15.42	1515.92	0.99997
Ablation period	0.02	−6.88	542.08	0.99945

Note: x indicates TB.

Figure 14 displays a graph of TB at 18.7 GHz V-pol versus ice thickness at different periods with a 1 mm radius of gas bubbles inside the ice during 2002–2003. Compared to the solid ice (no bubbles), the trends of TB and ice thickness were consistent, but there were differences in the details. In Tables 6–7, it is evident that the fits were weaker when there were bubbles inside the ice compared to the solid ice case, with smaller slopes for the linear fits and larger coefficients for the quadratic polynomials.

5   Discussion

The simulated TB of the HiGHTSI-MRT model varies across different periods, as shown in Figures 8–9. The most effective simulation was observed during the slow growth period, followed by the second-best performance during the growth period, and RMSE of 4.6 K was the lowest recorded. Simulation errors mainly occurred in the early growth period and the late ablation period, as shown in Figure 8. The uncertainties in the model mainly stemmed from the model's limitations, the forcing data, and the complex physical properties of lake ice.

Figure 14   Scatterplot of TB versus ice thickness for different periods during 2002–2003. The radius of the bubble inside the lake ice was set to 1 mm.

Table 7   Mean parameters fitted to TB and ice thickness for different periods with 1 mm radius bubbles inside lake ice during 2002–2011

Parameters	a	b	c	R^2
Formula		$H = bx + c$		
Growth period	\	1.32	−249.04	0.98628
Slow growth period	\	3.64	−788.30	0.98791
Ablation period	\	0.08	−387.94	0.940733
Formula		$H = ax^2 + bx + c$		
Growth period	0.01	−4.50	357.23	0.99965
Slow growth period	0.10	−43.52	4939.48	0.99971
Ablation period	0.03	−10.19	950.45	0.99479

Note: x indicates TB.

First, only the effects of bubble size and salinity on the physical properties of lake ice were considered in the model experiments. It's important to emphasize that the physical properties of lake ice are complex in natural conditions, including ice thickness, temperature, bubbles, salinity, correlation length, roughness, and ice porosity, affecting the microwave radiation of lake ice (Jezek et al., 1998; Leppäranta, 2023; Li et al., 2011; Murfitt et al., 2022, 2023; Veijola et al., 2024). Additionally, the model assumed homogeneity in each ice layer and did not consider the location or density of bubbles in it. During the early growth and late ablation periods, we found fluctuations in remotely sensed TB relative to the simulated TB. This may be due to the lake surface being an ice-water mixture influenced by liquid precipitation or melting during these periods, causing fluctuations in the remotely sensed TB. Also, during the late ablation period, a possible reason for the earlier decrease in the remotely sensed TB relative to the simulated TB could be ice drifting under the influence of strong winds. However, the HiGHTSI-MRT model did not account for the drift and consequent heat transfer. Furthermore, the simulations are affected by the input parameters. Although the reanalyzed meteorological data used in the study is of high quality, it may not fully reflect the real meteorological conditions which could reduce the accuracy of the simulation.

It is important to note that snow on ice can introduce uncertainty in the modeling of physical evolution of lake ice and microwave radiation transfer. The analysis above did not consider the effect of snow on simulated TB due to the insensitivity of the TB at 18.7 GHz V-pol to snow and the

shallowness of the snow cover on the ice surface in the Hulun Lake. Snow on ice changes the reflectance, absorbance, and transmittance assigned to the ice-snow interface by solar radiation, altering the light conditions under the ice and thereby affecting the temperature and rate of photosynthesis (Huang et al., 2021; Knoll et al., 2024). Due to its high albedo and low thermal conductivity, snow on ice plays a key role in controlling the energy exchange at the ice-air interface and influences the freeze-thaw process (Fujisaki-Manome et al., 2020; Leppäranta, 2014; Leppäranta et al., 2017; Oerlemans and Keller, 2023; Robinson et al., 2021). Properties of snow on ice, such as grain size, density and moisture, affect the backscatter and TB of microwave radiation on ice surface to varying degrees (Hallikainen et al., 2012, 2014; Jezek et al., 1998; Kwon et al., 2023; Stroeve et al., 2022; Veijola et al., 2024).

Therefore, future high-quality field studies of climate parameters and physical properties of lake ice as well as snow are needed. The next step in this study is to parameterize the combined model with lake ice field survey data to enhance the accuracy of the microwave radiation simulation and to explore the impact of additional physical properties of lake ice on TB. And the HiGHTSI-MRT model ought to be tested on other types of lakes with in situ data to provide broader application scenarios.

6 Conclusion

This study combined the microwave radiative transfer model SMRT with the thermodynamic ice model HIGHTSI to create a new model named HiGHTSI-MRT, which was applied to the thermal evolution and passive microwave radiation experiments on lake ice. Comparative analysis of the simulation results with the space-borne microwave TB data showed that the HiGHTSI-MRT can effectively simulate the evolution of the lake ice and TB, despite varying simulation accuracy between years.

The thermal evolution of lake ice could be understood in three stages, namely: the growth period, the slow growth period, and the ablation period. TB was affected by bubble size, temperature, and ice thickness. During the growth period when lake ice was thin, ice surface temperature had a greater impact on thickness and TB than air temperature. Therefore, incorporating ice surface temperature data into the lake ice inversion algorithm for different growth stages can improve its accuracy. TB at high frequency was sensitive to changes in thin ice, while TB at low frequency was sensitive to changes in thick ice. Overall, TB at 18.7 GHz V-pol performed the best, which is consistent with the results from comparisons of remotely sensed TB at different frequencies in Canadian lakes (Kang et al., 2010). The quadratic polynomial fit was found to be superior to the linear fit (average $R^2 > 0.999$). And the best fit was observed during the slow growth period. This suggests that the algorithm for retrieving ice thickness using TB is most applicable to the slow growth period and least applicable to

the ablation period.

This study has presented a methodology for simulating thermal processes and microwave radiation of lake ice. Although this study is not directly focused on the development of new technologies, we have constructed a combined model that can be applied in polar research, leading to a better understanding of how lake ice properties (e.g., bubbles, ice thickness, ice temperature, and salinity) affect TB of lake ice. Thus, we can exploit this forward modeling as a reference to enhance ice thickness inversion algorithms based on space-borne or airborne passive microwave data for Arctic sea ice and subarctic freshwater bodies.

References

Anheuser J, Liu Y H, Key J R. 2023. A climatology of thermodynamic vs. dynamic Arctic wintertime sea ice thickness effects during the CryoSat-2 era. Cryosphere, 17(7): 2871-2889, doi:10.5194/tc-17-2871-2023.

Bao H, Wang G M, Yao Y L, et al. 2021. Warming-driven shifts in ecological control of fish communities in a large northern Chinese lake over 66 years. Sci Total Environ, 770: 144722, doi:10.1016/j.scitotenv.2020.144722.

Brodzik M J, Long D G, Hardman M A, et al. 2016. MEaSUREs calibrated enhanced-resolution passive microwave daily EASE-grid 2.0 brightness temperature ESDR, version 1. Boulder: NASA National Snow and Ice Data Center Distributed Active Archive Center, doi:10.5067/MEASURES/CRYOSPHERE/NSIDC-0630.001.

Brown L C, Duguay C R. 2011. The fate of lake ice in the North American Arctic. Cryosphere, 5(4): 869-892, doi:10.5194/tc-5-869-2011.

Burgard C, Notz D, Pedersen L T, et al. 2020. The Arctic Ocean Observation Operator for 6.9 GHz (ARC3O)–Part 1: How to obtain sea ice brightness temperatures at 6.9 GHz from climate model output. Cryosphere, 14(7): 2369-2386, doi:10.5194/tc-14-2369-2020.

Cai Y, Duguay C R, Ke C Q. 2022. A 41-year (1979–2019) passive-microwave-derived lake ice phenology data record of the Northern Hemisphere. Earth Syst Sci Data, 14(7): 3329-3347, doi:10.5194/essd-14-3329-2022.

Cheng B, Vihma T, Pirazzini R, et al. 2006. Modelling of superimposed ice formation during the spring snowmelt period in the Baltic Sea. Ann Glaciol, 44: 139-146.

Cheng B, Vihma T, Rontu L, et al. 2014. Evolution of snow and ice temperature, thickness and energy balance in Lake Orajärvi, northern Finland. Tellus A Dyn Meteor Oceanogr, 66(1): 21564, doi:10.3402/tellusa.v66.21564.

Cheng Y B, Cheng B, Zheng F, et al. 2020. Air/snow, snow/ice and

ice/water interfaces detection from high-resolution vertical temperature profiles measured by ice mass-balance buoys on an Arctic lake. Ann Glaciol, 61(83): 309-319, doi:10.1017/aog.2020.51.

Dabboor M, Shokr M. 2021. Sensitivity of compact polarimetric SAR parameters to modeled lake ice growth. IEEE Trans Geosci Remote Sens, 59(12): 9953-9967, doi:10.1109/TGRS.2021.3050754.

Du J Y, Kimball J S, Duguay C, et al. 2017. Satellite microwave assessment of Northern Hemisphere lake ice phenology from 2002 to 2015. Cryosphere, 11(1): 47-63, doi:10.5194/tc-11-47-2017.

Duguay C R, Flato G M, Jeffries M O, et al. 2003. Ice-cover variability on shallow lakes at high latitudes: model simulations and observations. Hydrol Process, 17(17): 3465-3483, doi:10.1002/hyp.1394.

Engram M, Anthony K W, Meyer F J, et al. 2013. Characterization of L-band synthetic aperture radar (SAR) backscatter from floating and grounded thermokarst lake ice in Arctic Alaska. Cryosphere, 7(6): 1741-1752, doi:10.5194/tc-7-1741-2013.

Fan Y F, Li L L, Chen H H, et al. 2023. Evaluation and application of SMRT model for L-band brightness temperature simulation in Arctic sea ice. Remote Sens, 15(15): 3889, doi:10.3390/rs15153889.

Fujisaki-Manome A, Anderson E J, Kessler J A, et al. 2020. Simulating impacts of precipitation on ice cover and surface water temperature across large lakes. J Geophys Res Oceans, 125(5): 1-18, doi:10.1029/2019jc015950.

Fuller M C, Geldsetzer T, Yackel J, et al. 2015. Comparison of a coupled snow thermodynamic and radiative transfer model with *in situ* active microwave signatures of snow-covered smooth first-year sea ice. Cryosphere, 9(6): 2149-2161, doi:10.5194/tc-9-2149-2015.

Guo J, Zhang Y, Shi X, et al. 2022. Driving mechanisms of the evolution and ecological water demand of Hulun Lake in Inner Mongolia. Water, 14(21): 3415, doi:10.3390/w14213415.

Hallikainen M, Vaaja M, von Lerber A, et al. 2012. Multifrequency microwave radiometer measurements of snow on lake ice. Munich: 2012 IEEE International Geoscience and Remote Sensing Symposium, 142-145, doi:10.1109/IGARSS.2012.6351617.

Hallikainen M, Vaaja M, Seppänen J, et al. 2014. Brightness temperature behavior of snow on lake ice over a wide frequency range. Quebec City: 2014 IEEE Geoscience and Remote Sensing Symposium, 2411-2414, doi:10.1109/IGARSS.2014.6946958.

He J, Yang K, Tang W J, et al. 2020. The first high-resolution meteorological forcing dataset for land process studies over China. Sci Data, 7(1): 25, doi:10.1038/s41597-020-0369-y.

Huang W F, Zhang Z, Li Z J, et al. 2021. Under-ice dissolved oxygen and metabolism dynamics in a shallow lake: the critical role of ice and snow. Water Resour Res, 57(5): 1-16, doi:10.1029/2020wr027990.

Jezek K C, Perovich D K, Golden K M, et al. 1998. A broad spectral, interdisciplinary investigation of the electromagnetic properties of sea ice. IEEE Trans Geosci Remote Sens, 36(5): 1633-1641, doi:10.1109/36.718635.

Kang K K, Duguay C R, Howell S E L, et al. 2010. Sensitivity of AMSR-E brightness temperatures to the seasonal evolution of lake ice thickness. IEEE Geosci Remote Sens Lett, 7(4): 751-755, doi:10.1109/LGRS.2010.2044742.

Kang K K, Duguay C R, Lemmetyinen J, et al. 2014. Estimation of ice thickness on large northern lakes from AMSR-E brightness temperature measurements. Remote Sens Environ, 150: 1-19, doi:10.1016/j.rse.2014.04.016.

Karvonen J, Shi L J, Cheng B, et al. 2017. Bohai Sea ice parameter estimation based on thermodynamic ice model and earth observation data. Remote Sens, 9(3): 234, doi:10.3390/rs9030234.

Kawanishi T, Sezai T, Ito Y, et al. 2003. The Advanced Microwave Scanning Radiometer for the Earth Observing System (AMSR-E), NASDA's contribution to the EOS for global energy and water cycle studies. IEEE Trans Geosci Remote Sens, 41(2): 184-194, doi:10.1109/TGRS.2002.808331.

Kheyrollah Pour H, Duguay C R, Scott K A, et al. 2017. Improvement of lake ice thickness retrieval from MODIS satellite data using a thermodynamic model. IEEE Trans Geosci Remote Sens, 55(10): 5956-5965, doi:10.1109/TGRS.2017.2718533.

Knoll L B, Fry B, Hayes N M, et al. 2024. Reduced snow and increased nutrients show enhanced ice-associated photoautotrophic growth using a modified experimental under-ice design. Limnol Oceanog, 69(1): 203-216, doi:10.1002/lno.12469.

Kontu A, Lemmetyinen J, Pulliainen J, et al. 2014. Observation and modeling of the microwave brightness temperature of snow-covered frozen lakes and wetlands. IEEE Trans Geosci Remote Sens, 52(6): 3275-3288, doi:10.1109/TGRS.2013.2272077.

Kontu A, Lemmetyinen J, Vehviläinen J, et al. 2017. Coupling SNOWPACK-modeled grain size parameters with the HUT snow emission model. Remote Sens Environ, 194: 33-47, doi:10.1016/j.rse.2016.12.021.

Kwon Y J, Kim H C, Kim J M, et al. 2023. Sensitivity of passive microwave satellite observations to snow density and grain size over Arctic sea ice. IEEE Trans Geosci Remote Sens, 61: 4302810, doi:10.1109/TGRS.2023.3322401.

Larue F, Royer A, De Sève D, et al. 2018. Simulation and assimilation of passive microwave data using a snowpack model coupled to a calibrated radiative transfer model over northeastern Canada. Water Resour Res, 54(7): 4823-4848, doi:10.1029/2017wr022132.

Launiainen J, Cheng B. 1998. Modelling of ice thermodynamics in natural water bodies. Cold Reg Sci Technol, 27(3): 153-178, doi:10.1016/S0165-232X(98)00009-3.

Leppäranta M. 2014. Freezing of lakes and the evolution of their ice cover. Heidelberg: Springer Verlag, doi:10.1007/978-3-642-29081-7.

Leppäranta M. 2023. Ice phenology and thickness modelling for lake ice climatology. Water, 15(16): 2951, doi:10.3390/w15162951.

Leppäranta M, Lewis J E. 2007. Observations of ice surface temperature and thickness in the Baltic Sea. Int J Remote Sens, 28(17): 3963-3977, doi:10.1080/01431160601075616.

Leppäranta M, Wang K G. 2008. The ice cover on small and large lakes: scaling analysis and mathematical modelling. Hydrobiologia, 599(1): 183-189, doi:10.1007/s10750-007-9201-3.

Leppäranta M, Virta J, Huttula T. 2017. Hydrologian perusteet. Helsinki: Helsingin yliopisto, Fysiikan laitos, 2017, doi: 10.31885/2018.00021 (in Finnish).

Li X D, Long D, Huang Q, et al. 2022. The state and fate of lake ice thickness in the Northern Hemisphere. Sci Bull, 67(5): 537-546, doi:10.1016/j.scib.2021.10.015.

Li Z J, Huang W F, Jia Q, et al. 2011. Distributions of crystals and gas bubbles in reservoir ice during growth period. Water Sci Eng, 4(2): 204-211, doi:10.3882/j.issn.1674-2370.2011.02.008.

Lindenschmidt K E, Baulch H M, Cavaliere E. 2018. River and lake ice processes—impacts of freshwater ice on aquatic ecosystems in a

changing globe. Water, 10(11): 1586, doi:10.3390/w10111586.

Long D G, Brodzik M J, Hardman M A. 2019. Enhanced-resolution SMAP brightness temperature image products. IEEE Trans Geosci Remote Sens, 57(7): 4151-4163, doi:10.1109/TGRS.2018.2889427.

Mäkynen M, Cheng B, Similä M. 2013. On the accuracy of thin-ice thickness retrieval using MODIS thermal imagery over Arctic first-year ice. Ann Glaciol, 54(62): 87-96, doi:10.3189/2013aog62a166.

Ménard P, Duguay C R, Flato G M, et al. 2002. Simulation of ice phenology on Great Slave Lake, Northwest Territories, Canada. Hydrol Process, 16(18): 3691-3706, doi:10.1002/hyp.1230.

Michel B, Ramseier R O. 1971. Classification of river and lake ice. Can Geotech J, 8(1): 36-45, doi:10.1139/t71-004.

Murfitt J, Duguay C R, Picard G, et al. 2022. Investigating the effect of lake ice properties on multifrequency backscatter using the snow microwave radiative transfer model. IEEE Trans Geosci Remote Sens, 60: 4305623, doi:10.1109/TGRS.2022.3197109.

Murfitt J, Duguay C, Picard G, et al. 2023. Forward modelling of synthetic aperture radar backscatter from lake ice over Canadian subarctic lakes. Remote Sens Environ, 286: 113424, doi:10.1016/j.rse.2022.113424.

Murfitt J, Duguay C, Picard G, et al. 2024. Forward modelling of synthetic-aperture radar (SAR) backscatter during lake ice melt conditions using the Snow Microwave Radiative Transfer (SMRT) model. Cryosphere, 18(2): 869-888, doi:10.5194/tc-18-869-2024.

Newton A M W, Mullan D J. 2021. Climate change and Northern Hemisphere lake and river ice phenology from 1931–2005. Cryosphere, 15(5): 2211-2234, doi:10.5194/tc-15-2211-2021.

Oerlemans J, Keller F. 2023. Application of a simple model for ice growth to the Lake St. Moritz, Switzerland. J Glaciol, 69(276): 1085-1090, doi:10.1017/jog.2022.110.

Pan J M, Jiang L M, Zhang L X, et al. 2011. Simulation of emission properties and snow-soil system status of a melting thin snow pack. Vancouver: 2011 IEEE International Geoscience and Remote Sensing Symposium, 3198-3201, doi:10.1109/IGARSS.2011.6049899.

Picard G, Sandells M, Löwe H. 2018. SMRT: an active–passive microwave radiative transfer model for snow with multiple microstructure and scattering formulations (v1.0). Geosci Model Dev, 11(7): 2763-2788, doi:10.5194/gmd-11-2763-2018.

Rees W G. 2005. Remote sensing of snow and ice. Boca Raton: CRC Press.

Robinson A L, Ariano S S, Brown L C. 2021. The influence of snow and ice albedo towards improved lake ice simulations. Hydrology, 8(1): 11, doi:10.3390/hydrology8010011.

Rostosky P, Spreen G, Gerland S, et al. 2020. Modeling the microwave emission of snow on Arctic sea ice for estimating the uncertainty of satellite retrievals. J Geophys Res Oceans, 125(3): 1-16, doi:10.1029/2019jc015465.

Semmler T, Cheng B, Yang Y, et al. 2012. Snow and ice on Bear Lake (Alaska)–sensitivity experiments with two lake ice models. Tellus A Dyn Meteor Oceanogr, 64(1): 17339, doi:10.3402/tellusa.v64i0.17339.

Sharma S, Blagrave K, Magnuson J J, et al. 2019. Widespread loss of lake ice around the Northern Hemisphere in a warming world. Nat Clim Change, 9: 227-231, doi:10.1038/s41558-018-0393-5.

Similä M, Mäkynen M, Cheng B, et al. 2013. Multisensor data and thermodynamic sea-ice model based sea-ice thickness chart with application to the Kara Sea, Arctic Russia. Ann Glaciol, 54(62): 241-252, doi:10.3189/2013aog62a163.

Singh R K, Oza S R, Vyas N K, et al. 2011. Estimation of thin ice thickness from the advanced microwave scanning radiometer-EOS for

coastal polynyas in the Chukchi and Beaufort seas. IEEE Trans Geosci Remote Sens, 49(8): 2993-2998, doi:10.1109/TGRS.2011.2123101.

Stroeve J, Nandan V, Willatt R, et al. 2022. Rain on snow (ROS) understudied in sea ice remote sensing: a multi-sensor analysis of ROS during MOSAiC (Multidisciplinary drifting Observatory for the Study of Arctic Climate). Cryosphere, 16(10): 4223-4250, doi:10.5194/tc-16-4223-2022.

Surdyk S. 2002. Using microwave brightness temperature to detect short-term surface air temperature changes in Antarctica: an analytical approach. Remote Sens Environ, 80(2): 256-271, doi:10.1016/S0034-4257(01)00308-X.

Tonboe R T. 2010. The simulated sea ice thermal microwave emission at window and sounding frequencies. Tellus A Dyn Meteor Oceanogr, 62(3): 333-344, doi:10.1111/j.1600-0870.2010.00434.x.

Tonboe R T, Dybkjær G, Høyer J L. 2011. Simulations of the snow covered sea ice surface temperature and microwave effective temperature. Tellus A Dyn Meteor Oceanogr, 63(5): 1028, doi:10.1111/j.1600-0870.2011.00530.x.

Vargel C, Royer A, St-Jean-Rondeau O, et al. 2020. Arctic and subarctic snow microstructure analysis for microwave brightness temperature simulations. Remote Sens Environ, 242: 111754, doi:10.1016/j.rse.2020.111754.

Veijola K, Cohen J, Mäkynen M, et al. 2024. X- and Ku-band SAR backscattering signatures of snow-covered lake ice and sea ice. Remote Sens, 16(2): 369, doi:10.3390/rs16020369.

Walsh S E, Vavrus S J, Foley J A, et al. 1998. Global patterns of lake ice phenology and climate: Model simulations and observations. J Geophys Res, 103(D22): 28825-28837, doi:10.1029/98jd02275.

Wang L, Du Z H, Wei Z Q, et al. 2023. Large methane emission during ice-melt in spring from thermokarst lakes and ponds in the interior Tibetan Plateau. CATENA, 232: 107454, doi:10.1016/j.catena.2023.107454.

Wang X C, Feng L, Gibson L, et al. 2021. High-resolution mapping of ice cover changes in over 33, 000 lakes across the North Temperate Zone. Geophys Res Lett, 48: e2021GL095614, doi:10.1029/2021gl095614.

Wang X J, Key J R, Liu Y H. 2010. A thermodynamic model for estimating sea and lake ice thickness with optical satellite data. J Geophys Res, 115(C12): C12035, doi:10.1029/2009jc005857.

Wang X X, Qiu Y B, Zhang Y X, et al. 2022. A lake ice phenology dataset for the Northern Hemisphere based on passive microwave remote sensing. Big Earth Data, 6(4): 401-419, doi:10.1080/20964471.2021.1992916.

Warren S G. 2019. Optical properties of ice and snow. Phil Trans R Soc A, 377(2146): 20180161, doi:10.1098/rsta.2018.0161.

Willmes S, Nicolaus M, Haas C. 2014. The microwave emissivity variability of snow covered first-year sea ice from late winter to early summer: a model study. Cryosphere, 8(3): 891-904, doi:10.5194/tc-8-891-2014.

Wu Q H, Li C Y, Sun B, et al. 2019. Change of ice phenology in the Hulun Lake from 1986 to 2017. Prog Geogr, 38(12): 1933-1943, doi:10.18306/dlkxjz.2019.12.009.

Yang F, Cen R, Feng W, et al. 2021. Dynamic simulation of nutrient distribution in lakes during ice cover growth and ablation. Chemosphere, 281: 130781, doi:10.1016/j.chemosphere.2021.130781.

Yang Y, Leppäranta M, Cheng B, et al. 2012. Numerical modelling of snow and ice thicknesses in Lake Vanajavesi, Finland. Tellus A Dyn Meteor Oceanogr, 64(1): 17202, doi:10.3402/tellusa.v64i0.17202.

Supplementary Tables

Table S1   Information on simulated and satellite altimetry ice thickness in Hulun Lake during 2002−2011

Date	Observed ice thickness/cm	Simulated ice thickness/cm
2003-02-27	125.9	113.6
2003-03-09	137.6	117.8
2003-03-18	134.5	120.4
2003-03-28	142.6	123.3
2004-02-09	113.7	106.5
2004-02-29	123.5	117.9
2004-03-09	134.1	121.9
2004-03-19	135.6	125.7
2007-12-28	70.5	65.5
2008-02-25	110.4	117.0
2008-04-15	89.4	123.4
2008-11-29	46.0	5.1
2008-12-09	55.2	10.1
2008-12-19	68.6	18.6
2008-12-29	81.1	29.8
2009-12-01	55.4	20.4
2009-12-11	71.7	29.5
2009-12-20	71.1	41.6
2011-01-01	61.8	47.4
2011-01-11	62.2	57.3
2011-01-21	63.8	67.0
2011-01-31	58.3	74.8
2011-03-22	77.8	96.9

Table S2   RMSE (unit: K) of simulated TB and CETB in different periods (the best simulation performances are in bold). I, the growth period; II, the slow growth period; III, the ablation period; IS, the ice season

	2002				2003				2004			
	I	II	III	IS	I	II	III	IS	I	II	III	IS
0 mm	24.9	15.8	21.3	20.6	17.1	15.2	**25.1**	18.5	31.2	15.5	**25.7**	23.5
0.25 mm	24.8	15.5	21.1	20.4	17.0	14.9	25.1	18.3	31.1	15.2	25.8	23.3
0.50 mm	24.2	13.6	20.2	19.3	16.0	13.0	25.1	17.4	30.4	13.4	26.4	22.6
0.75 mm	22.9	10.1	**19.2**	17.5	14.2	8.1	26.0	16.2	**16.6**	10.4	28.2	21.6
1.00 mm	21.3	**7.9**	19.6	**16.4**	12.7	**8.0**	28.1	**16.2**	27.3	**8.9**	31.2	**21.2**
1.25 mm	20.1	8.2	21.4	16.4	**12.5**	8.5	30.5	17.3	25.6	9.5	34.4	21.5
1.50 mm	19.2	9.1	23.6	16.9	13.0	9.5	32.5	18.4	24.1	10.4	36.7	21.8
1.75 mm	18.5	9.9	25.3	17.4	13.6	10.3	33.8	19.3	23.0	11.2	38.2	22.0
2.00 mm	18.0	10.4	26.6	17.8	14.1	10.8	34.8	19.9	22.1	11.7	39.2	22.2
2.25 mm	**17.8**	10.7	27.6	18.1	14.8	11.1	35.5	20.4	21.4	11.9	40.1	22.3
2.50 mm	17.9	10.7	28.4	18.4	15.7	11.0	36.3	20.9	21.1	12.0	41.1	22.6
2.75 mm	18.2	10.6	29.1	18.7	16.9	10.9	37.0	21.4	20.9	12.0	42.2	22.9
3.00 mm	18.6	10.7	29.7	19.1	18.1	10.9	37.7	22.0	20.9	12.2	43.2	23.2
Salinity 1‰	\	\	\	\	\	\	\	\	\	\	\	\

Continued

	2005				2006				2007			
	I	II	III	IS	I	II	III	IS	I	II	III	IS
0 mm	41.7	17.9	**25.2**	28.8	61.6	29.2	19.5	43.4	44.9	18.8	**27.0**	28.8
0.25 mm	41.6	17.6	25.3	28.6	61.5	28.9	19.3	43.2	44.9	18.5	27.1	28.7
0.50 mm	40.6	15.5	25.8	27.7	60.7	26.8	17.9	42.0	44.2	16.6	27.9	28.0
0.75 mm	38.5	11.7	27.5	26.1	58.7	22.6	15.4	39.6	42.9	13.2	30.1	26.9
1.00 mm	35.7	8.5	30.5	24.8	56.0	17.9	13.5	36.8	40.9	10.7	33.4	**26.3**
1.25 mm	33.1	**7.5**	33.6	24.3	53.1	14.6	**13.5**	34.4	38.8	**10.4**	36.8	26.4
1.50 mm	30.9	8.2	36.0	24.1	50.3	13.3	14.6	32.6	36.8	11.3	39.3	26.7
1.75 mm	29.0	9.4	37.7	24.0	47.9	13.2	16.0	31.3	35.1	12.2	41.0	26.8
2.00 mm	27.4	10.3	38.8	24.0	45.9	13.4	17.3	30.3	33.5	12.9	42.1	26.9
2.25 mm	26.1	10.6	39.8	23.9	44.1	13.3	18.3	29.4	32.2	13.2	43.1	26.9
2.50 mm	25.0	10.1	40.7	23.7	42.5	12.6	19.3	28.4	31.1	13.2	44.2	26.9
2.75 mm	24.1	9.2	41.7	23.6	41.1	11.5	20.2	27.5	30.2	13.0	45.4	27.0
3.00 mm	**23.4**	8.2	42.7	**23.5**	**39.8**	10.3	21.0	**26.6**	**29.5**	12.8	46.6	27.2
Salinity 1‰	\	\	\	\	46.7	**7.1**	18.0	29.8	\	\	\	\

	2008				2009				2010			
	I	II	III	IS	I	II	III	IS	I	II	III	IS
0 mm	81.6	69.1	**53.8**	71.1	60.2	25.2	19.5	42.3	61.3	36.1	20.6	44.9
0.25 mm	81.5	69.0	53.8	71.0	60.0	24.8	19.3	42.1	61.2	35.8	20.4	44.7
0.50 mm	81.0	68.5	54.0	70.6	59.0	22.7	18.5	40.8	60.6	33.7	19.1	43.5
0.75 mm	79.9	67.6	54.5	69.9	56.7	18.7	17.3	38.4	59.2	29.5	16.9	41.1
1.00 mm	78.4	67.0	55.6	69.2	53.5	14.7	**16.9**	35.6	57.1	24.4	**15.7**	38.3
1.25 mm	76.8	66.8	56.9	68.7	50.1	12.5	17.5	33.2	54.7	20.2	16.5	35.9
1.50 mm	75.3	**66.7**	58.0	68.3	47.0	12.4	18.5	31.4	52.2	17.9	18.1	34.1
1.75 mm	74.1	66.7	58.8	68.0	44.3	13.4	19.6	30.1	49.9	17.0	19.5	32.7
2.00 mm	73.2	66.7	59.5	67.7	42.0	14.3	20.6	29.0	47.9	16.6	20.6	31.7
2.25 mm	72.3	66.7	60.1	67.5	39.9	14.5	21.6	28.0	46.1	16.1	21.5	30.7
2.50 mm	71.7	66.7	60.8	67.4	38.1	13.8	22.6	27.0	44.5	15.1	22.3	29.7
2.75 mm	71.1	66.8	61.6	**67.3**	36.5	12.6	23.6	25.8	43.1	13.8	23.0	28.8
3.00 mm	**70.6**	66.9	62.4	67.3	**35.0**	11.2	24.6	**24.8**	**41.9**	12.3	23.7	**27.9**
Salinity 1‰	73.8	67.7	61.7	68.7	42.8	**4.6**	23.0	28.2	49.3	**9.1**	21.9	31.1

Table S3 The correlation coefficients between ice temperature and TB. I, the growth period; II, the slow growth period; III, the ablation period; IS, the ice season

Ice thickness/cm	6.9 GHz V-pol				6.9 GHz H-pol			
	I	II	III	IS	I	II	III	IS
0	−0.90	0.77	−0.75	−0.08	−0.91	0.76	−0.74	−0.08
10	−0.96	0.80	−0.85	0.00	−0.96	0.80	−0.85	−0.01
20	−0.98	0.77	−0.79	−0.11	−0.98	0.77	−0.79	−0.11
30	−0.99	0.73	−0.83	0.22	−0.99	0.73	−0.82	0.21
40	−0.99	0.65	−0.85	−0.14	−0.99	0.65	−0.85	−0.14
50	−0.99	0.50	−0.88	−0.13	−0.99	0.50	−0.88	−0.13
60	−1.00	0.22	−0.90	−0.19	−1.00	0.22	−0.90	−0.19
70	\	−0.25	−0.91	−0.20	\	−0.25	−0.91	−0.20
80	\	−0.37	−0.94	−0.28	\	−0.37	−0.94	−0.28
90	\	−0.38	−0.95	−0.34	\	−0.38	−0.95	−0.34
100	\	−0.57	−0.99	−0.47	\	−0.58	−0.99	−0.47
110	\	−0.83	−1.00	−0.79	\	−0.83	−1.00	−0.79
120	\	−0.98	−1.00	−0.96	\	−0.98	−1.00	−0.96

Continued

Ice thickness/cm	10.6 GHz V-pol				10.6 GHz H-pol			
	I	II	III	IS	I	II	III	IS
0	−0.91	0.76	−0.74	−0.09	−0.91	0.76	−0.74	−0.10
10	−0.96	0.79	−0.84	−0.01	−0.97	0.79	−0.84	−0.02
20	−0.98	0.77	−0.78	−0.12	−0.98	0.77	−0.78	−0.12
30	−0.99	0.72	−0.82	0.21	−0.99	0.72	−0.82	0.20
40	−0.99	0.65	−0.85	−0.15	−0.99	0.64	−0.85	−0.15
50	−0.99	0.50	−0.87	−0.13	−0.99	0.49	−0.87	−0.14
60	−1.00	0.21	−0.89	−0.19	−1.00	0.21	−0.89	−0.20
70	\	−0.26	−0.91	−0.20	\	−0.26	−0.91	−0.21
80	\	−0.38	−0.94	−0.28	\	−0.38	−0.94	−0.28
90	\	−0.39	−0.95	−0.34	\	−0.39	−0.95	−0.35
100	\	−0.58	−0.99	−0.47	\	−0.58	−0.99	−0.47
110	\	−0.83	−1.00	−0.79	\	−0.83	−1.00	−0.79
120	\	−0.98	−1.00	−0.96	\	−0.98	−1.00	−0.96

Ice thickness/cm	18.7 GHz V-pol				18.7 GHz H-pol			
	I	II	III	IS	I	II	III	IS
0	−0.92	0.74	−0.72	−0.13	−0.92	0.74	−0.71	−0.14
10	−0.97	0.78	−0.80	−0.05	−0.97	0.77	−0.80	−0.05
20	−0.98	0.75	−0.75	−0.15	−0.98	0.75	−0.74	−0.16
30	−0.99	0.70	−0.79	0.16	−0.99	0.70	−0.78	0.16
40	−0.99	0.62	−0.82	−0.18	−0.99	0.62	−0.82	−0.18
50	−0.99	0.47	−0.85	−0.16	−0.99	0.46	−0.85	−0.17
60	−1.00	0.18	−0.87	−0.22	−1.00	0.17	−0.87	−0.22
70	\	−0.30	−0.89	−0.22	\	−0.30	−0.89	−0.23
80	\	−0.41	−0.93	−0.30	\	−0.41	−0.93	−0.30
90	\	−0.41	−0.94	−0.36	\	−0.42	−0.94	−0.36
100	\	−0.59	−0.98	−0.48	\	−0.60	−0.98	−0.48
110	\	−0.84	−1.00	−0.80	\	−0.84	−1.00	−0.80
120	\	−0.98	−1.00	−0.96	\	−0.98	−1.00	−0.96

Ice thickness/cm	23.8 GHz V-pol				23.8 GHz H-pol			
	I	II	III	IS	I	II	III	IS
0	−0.93	0.72	−0.69	−0.16	−0.93	0.72	−0.69	−0.17
10	−0.97	0.76	−0.77	−0.08	−0.97	0.75	−0.76	−0.08
20	−0.98	0.73	−0.71	−0.18	−0.98	0.73	−0.70	−0.19
30	−0.99	0.68	−0.76	0.12	−0.99	0.68	−0.75	0.12
40	−0.99	0.60	−0.80	−0.21	−0.99	0.59	−0.80	−0.21
50	−0.99	0.44	−0.83	−0.19	−0.99	0.44	−0.83	−0.19
60	−1.00	0.14	−0.86	−0.24	−1.00	0.14	−0.86	−0.24
70	\	−0.33	−0.88	−0.24	\	−0.33	−0.88	−0.24
80	\	−0.44	−0.92	−0.31	\	−0.44	−0.91	−0.31
90	\	−0.44	−0.93	−0.37	\	−0.44	−0.93	−0.37
100	\	−0.61	−0.98	−0.48	\	−0.61	−0.98	−0.48
110	\	−0.85	−1.00	−0.80	\	−0.85	−1.00	−0.80
120	\	−0.98	−1.00	−0.96	\	−0.98	−1.00	−0.96

Continued

Ice thickness/cm	36.5 GHz V-pol				36.5 GHz H-pol			
	I	II	III	IS	I	II	III	IS
0	−0.95	0.65	−0.56	−0.25	−0.96	0.65	−0.56	−0.25
10	−0.98	0.68	−0.62	−0.16	−0.98	0.68	−0.62	−0.16
20	−0.99	0.65	−0.56	−0.27	−0.99	0.65	−0.56	−0.27
30	−0.99	0.60	−0.64	−0.01	−0.99	0.60	−0.64	−0.01
40	−0.99	0.50	−0.71	−0.29	−0.99	0.50	−0.71	−0.29
50	−0.99	0.34	−0.76	−0.26	−0.99	0.34	−0.76	−0.26
60	−1.00	0.03	−0.79	−0.31	−1.00	0.03	−0.79	−0.31
70	\	−0.44	−0.81	−0.30	\	−0.44	−0.81	−0.30
80	\	−0.53	−0.87	−0.36	\	−0.53	−0.87	−0.36
90	\	−0.52	−0.89	−0.41	\	−0.52	−0.89	−0.41
100	\	−0.66	−0.96	−0.50	\	−0.66	−0.97	−0.50
110	\	−0.87	−0.99	−0.82	\	−0.87	−0.99	−0.82
120	\	−0.98	−1.00	−0.96	\	−0.98	−1.00	−0.96

Ice thickness/cm	89.0 GHz V-pol				89.0 GHz H-pol			
	I	II	III	IS	I	II	III	IS
0	−0.88	−0.60	−0.24	−0.35	−0.89	−0.60	−0.24	−0.35
10	−0.56	−0.62	0.55	−0.13	−0.65	−0.62	0.39	−0.16
20	0.07	−0.59	0.53	0.13	−0.39	−0.59	0.40	−0.05
30	0.98	−0.53	0.55	−0.14	0.97	−0.53	0.58	−0.23
40	0.99	−0.43	0.61	0.34	0.99	−0.43	0.62	0.34
50	0.98	−0.26	0.68	0.31	0.98	−0.26	0.69	0.31
60	0.99	0.05	0.73	0.36	0.99	0.05	0.74	0.36
70	\	0.51	0.76	0.35	\	0.51	0.76	0.35
80	\	0.59	0.82	0.40	\	0.59	0.83	0.40
90	\	0.57	0.86	0.43	\	0.57	0.86	0.43
100	\	0.70	0.95	0.51	\	0.70	0.95	0.51
110	\	0.88	0.99	0.83	\	0.88	0.99	0.83
120	\	0.99	0.99	0.96	\	0.99	0.99	0.96